REGENERATION

Immunomodulatory role of the stem cell circadian clock in muscle repair

Pei Zhu[1,2], Eric M. Pfrender[1,2], Adam W. T. Steffeck[1,2], Colleen R. Reczek[3], Yalu Zhou[4,5], Abhishek Vijay Thakkar[1,2], Neha R. Gupta[1,2], Ariana Kupai[1,2], Amber Willbanks[6], Richard L. Lieber[6,7,8], Ishan Roy[6,7,9], Navdeep S. Chandel[1,3], Clara B. Peek[1,2]*

Circadian rhythms orchestrate physiological processes such as metabolism, immune function, and tissue regeneration, aligning them with the optimal time of day (TOD). This study identifies an interplay between the circadian clock within muscle stem cells (SCs) and their capacity to modulate the immune microenvironment during muscle regeneration. We reveal that the SC clock triggers TOD–dependent inflammatory gene transcription after injury, particularly genes related to neutrophil activity and chemotaxis. These responses are driven by cytosolic regeneration of the signaling metabolite nicotinamide adenine dinucleotide (oxidized form) (NAD^+), as enhancing cytosolic NAD^+ regeneration in SCs is sufficient to induce inflammatory responses that influence muscle regeneration. Mononuclear single-cell sequencing of the regenerating muscle niche further implicates the cytokine CCL2 in mediating SC-neutrophil cross-talk in a TOD-dependent manner. Our findings highlight the intersection between SC metabolic shifts and immune responses within the muscle microenvironment, dictated by circadian rhythms, and underscore the potential for targeting circadian and metabolic pathways to enhance tissue regeneration.

INTRODUCTION

The circadian clock, the body's intrinsic time-keeping mechanism, operates through a molecular clock in almost all cells within the body (*1*). It comprises a central clock in the brain's hypothalamic suprachiasmatic nucleus and peripheral clocks distributed throughout the rest of the body, influencing behaviors like sleep and physiological processes including core body temperature, hormone secretion, immune function, and metabolism (*2*, *3*). Circadian rhythms ensure that these activities align optimally with the time of day (TOD), maximizing fitness. On the molecular level, the clock functions as a transcription-translation feedback loop consisting of activators (CLOCK and BMAL1) that direct the expression of thousands of genes, including their own repressors (PER1-3 and CRY1-2). Accessory proteins can stabilize the oscillation, including the nuclear receptors, REVERBa/b and RORa/b (*1*). Previous work from our group (*4*) and others (*5*) uncovered that the efficiency of muscle repair is subject to TOD variations, suggesting that circadian rhythms influence tissue regeneration. We also demonstrated that muscle stem cell–specific deletion of *Bmal1* impairs hypoxic growth and differentiation of myoblasts in vitro and hinders muscle regeneration in vivo (*4*). Despite these findings, the underlying mechanisms by which SC circadian clocks regulate muscle repair remain largely unknown.

Muscle regeneration is a highly coordinated, dynamic process involving intricate interactions between muscle stem cells (SCs, a.k.a. satellite cells) and the immune system (*6*). SCs are crucial for muscle repair, activated by injury to proliferate and differentiate, thereby replenishing the muscle fiber pool (*7*). Neutrophils, the first responders to injury, play a critical role in initiating repair by clearing debris and secreting cytokines and chemokines (*8*), thus fostering an environment conducive to healing and influencing the behavior of SCs and other progenitor cells (*9*, *10*). Nevertheless, the interactions between neutrophils and SCs, especially considering the metabolic changes triggered by muscle injury, are yet to be fully understood.

This study identifies a role for the SC circadian clock in modulating these interactions through metabolic responses to injury. We demonstrate that the SC clock drives the redox cycling of the oxidized form of nicotinamide adenine dinucleotide (NAD^+) via anaerobic glycolysis in a TOD-dependent manner. Using a genetic mouse model expressing the cytosolic reduced form of NAD^+ (NADH) oxidase from *Lactobacillus brevis* (*LbNOX*) within SCs, we found that cytoplasmic NAD^+ regeneration is sufficient to boost myofiber repair. Notably, we uncovered a previously unrecognized role for NAD^+ regeneration in SCs in the activity of poly[adenosine diphosphate (ADP)–ribose] polymerase 1 (PARP1) and nuclear factor κB (NF-κB), extending beyond previously identified NAD^+-dependent control of Sirtuins (SIRTs) and myogenic gene deacetylation. We show that hypoxic NAD^+ regeneration acts in SCs to drive neutrophil chemotaxis–related gene expression and enhance neutrophil infiltration and their interaction with SCs. In particular, the NAD^+-regulated chemokine *Ccl2* exhibited varied expression levels across different times of day, influencing the quality and rate of muscle regeneration.

Our findings not only provide insights into the circadian regulation of muscle regeneration but also highlight a complex metabolic-immune interface within the muscle microenvironment, potentially explaining the compromised muscle regeneration observed in conditions characterized by disrupted circadian rhythms, such as obesity, diabetes, and aging.

RESULTS

ASCs express genes modulating anaerobic glycolysis and neutrophil functions

Under conditions of hypoxia, pyruvate, the end product of glycolysis, is converted into lactate by lactate dehydrogenase A (Ldha). This

[1]Department of Biochemistry and Molecular Genetics, Northwestern University Feinberg School of Medicine, Chicago, IL, USA. [2]Department of Medicine, Division of Endocrinology, Metabolism and Molecular Medicine, Northwestern University Feinberg School of Medicine, Chicago, IL, USA. [3]Department of Medicine, Division of Pulmonary and Critical Care, Northwestern University Feinberg School of Medicine, Chicago, IL, USA. [4]Division of Nephrology and Hypertension, Northwestern University Feinberg School of Medicine, Chicago, IL, USA. [5]Feinberg Cardiovascular and Renal Research Institute, Chicago, IL, USA. [6]Shirley Ryan AbilityLab (formerly known as Rehabilitation Institute of Chicago), Chicago, IL, USA. [7]Department of Physical Medicine and Rehabilitation, Northwestern University, Chicago, IL, USA. [8]Hines VA Hospital, Maywood, IL, USA. [9]Robert H. Lurie Comprehensive Cancer Center, Northwestern University, Chicago, IL, USA.
*Corresponding author. Email: c-peek@northwestern.edu

process involves the reduction of pyruvate with electrons from NADH, facilitating the regeneration of NAD^+ (Fig. 1A). Using the myotoxin cardiotoxin to injure mouse muscles, we observed that the injury creates an acute hypoxic environment within skeletal muscle, a condition confirmed by the substantial stabilization of hypoxia-inducible factor (HIF) proteins in the initial days post-injury (fig. S1A). SCs within the muscle are also subjected to this hypoxic stress, as demonstrated by microarray analysis from a previous study (*9*) that examined the temporal gene expression in SCs under both homeostatic conditions and after cardiotoxin-induced injury at various time points. Key HIF target genes, such as *Hk2*, *Vegfa*, and *Epo*, were markedly up-regulated in SCs by day 2 post-injury, followed by a decline over time (fig. S1B).

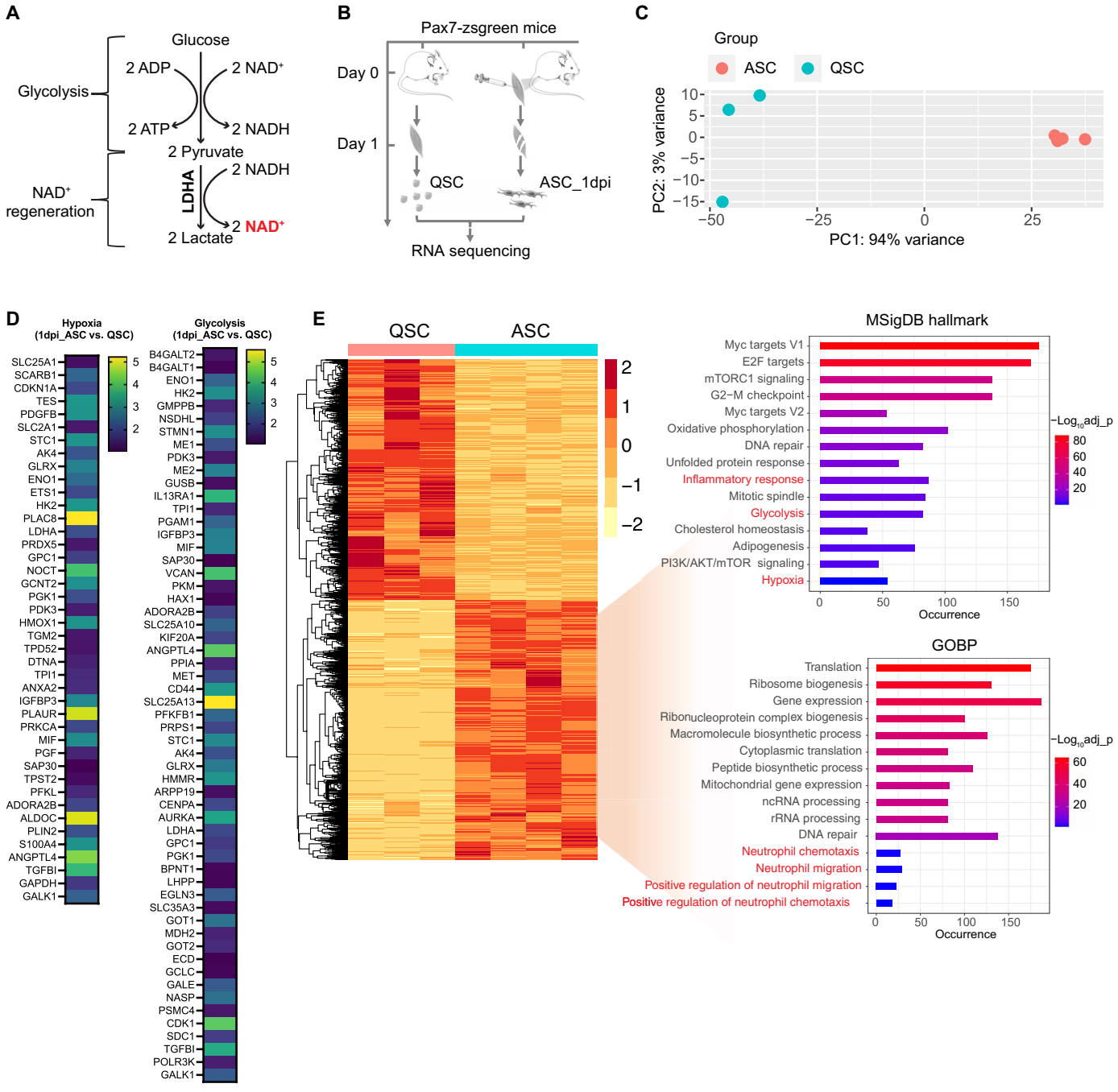

Fig. 1. Elevated expression of glycolysis and inflammation-related genes in SCs following CTX injury. (**A**) Schematic representation of the anaerobic glycolysis pathway. (**B**) Schematic diagram of experiment using SCs extracted from the hindlimb muscles of Pax7-zsgreen mice, both uninjured and following cardiotoxin-induced injury at ZT16, on day 1 post-injury, and subjected to RNA sequencing for transcriptome analysis. (**C**) Principal components analysis depicting the transcriptional disparities between ASCs at 1 dpi and QSCs. (**D**) Heatmap showing genes significantly up-regulated (adjusted *P* value <0.05) in ASCs at 1 dpi, highlighting associations with hypoxia and glycolysis, in comparison to QSCs. The color scale represents the $\log_2$ fold change, indicating the magnitude of gene expression changes. (**E**) Pathway enrichment analysis, using MSigDB hallmarks and gene ontology biological processes, for genes significantly up-regulated (adjusted *P* value <0.05) in ASCs at 1 dpi relative to QSCs.

Table 1. Reagent table. List and source information for reagents and resources used in the study.

Reagent or resource	Source	Identifier
Antibodies		
Biotin anti-CD31	BioLegend	Catalog no. 102404
Biotin anti-CD45	BioLegend	Catalog no. 103104
Biotin anti-Sca1	BioLegend	Catalog no. 108104
PE anti-VCAM1	Miltenyi Biotec	Catalog no. 130-104-712
Anti-laminin	Sigma-Aldrich	Catalog no. L9393
Ly-6G (Gr-1) antibody	Thermo Fisher Scientific	Catalog no. 14-5931-82
Poly(ADP-ribose) polyclonal antibody	Eno Life Science	Catalog no. ALX-210-890A-0100
Goat anti-rabbit IgG secondary antibody, Alexa Fluor 488	Thermo Fisher Scientific	Catalog no. A11034
Goat anti-rat IgG secondary antibody, Alexa Fluor 555	Thermo Fisher Scientific	Catalog no. A-21434
Goat anti-rabbit IgG secondary antibody, Alexa Fluor 594	Thermo Fisher Scientific	Catalog no. A11012
Anti-HIF1α	Cayman	Catalog no. 10006421
PAR/pADPr	R&D Systems	Catalog no. 4335-MC-100
Anti–NF-κB p65	Cell Signaling Technology	Catalog no. 8242S
Anti–phospho–NF-κB p65 (Ser^{536})	Cell Signaling Technology	Catalog no. 3033S
β-Actin	Cell Signaling Technology	Catalog no. 4970
InVivoMab anti-mouse Ly6G	BioXCell	Catalog no. BE0075-1
InVivoMab anti-trinitrophenol Isotype control rat monoclonal	BioXCell	Catalog no. BE0089
Chemicals, consumables		
Tamoxifen	Sigma-Aldrich	Catalog no. T5648
Cardiotoxin	Millipore Sigma	Catalog no. 217503-1MG
Insulin syringes	BD	Catalog no. BD-25150
Tissue Plus O.C.T. compound	Thermo Fisher Scientific	Catalog no. 23-730-571
Formalin	Thermo Fisher Scientific	Catalog no. MR0458682
Clarifier	Sigma-Aldrich	Catalog no. A3179
Hematoxylin	Thermo Fisher Scientific	Catalog no. 72-11 L
Eosin-Y	Thermo Fisher Scientific	Catalog no.71-11 L
Permount mounting medium	Electron Microscopy Science	Catalog no. 17986-01
4% Paraformaldehyde	Boster Bio	Catalog no. AR1068
VectaShield HardSet antifade mounting medium with DAPI	Vector Laboratories	Catalog no. H-1500-10
Propidium iodide Ready Flow reagent	Thermo Fisher Scientific	Catalog no. R37169
Hams F-10 medium	Corning	Catalog no. 10-070-CV
DMEM	Corning	Catalog no. 90-013-PB
Collagenase D	Roche	Catalog no. 11088866001
Dispase II	Gibco	Catalog no. 17105041
40-μm cell strainer	Corning	Catalog no. 07-201-430
70-μm cell strainer	Corning	Catalog no. 352350
Pre-sort buffer	BD	Catalog no. BD-B563503
Matrigel matrix	Corning	Catalog no. 356231
Basic fibroblast growth factor	ProSpec	Catalog no. CYT-218
Ad-CMV-iCre	Vector Biolabs	Catalog no. 1045
Ad-CMV-Null	Vector Biolabs	Catalog no. 1300
Fetal bovine serum	Corning	Catalog no. 35-010-CV
AMPure XP beads	Beckman Coulter	Catalog no. A63880
CelLytic mammalian tissue lysis reagent	Sigma-Aldrich	Catalog no. C3228
Protease inhibitor cocktail	Sigma-Aldrich	Catalog no. P8340
DC protein assay kit	Bio-Rad	Catalog no. 5000111
0.45-μm nitrocellulose membrane	Bio-Rad	Catalog no. 1620115
RBC lysis buffer (10X)	BioLegend	Catalog no. 420301

(*Continued*)

(*Continued*)

Reagent or resource	Source	Identifier
BGP15	Tocris	Catalog no. 6703
EB 47	Tocris	Catalog no. 4140
Galloflavin	Tocris	Catalog no. 4795
Mouse Ccl2 cDNA ORF clone	GenScript	Catalog no. OMu19558
Phusion high-fidelity DNA polymerase and dNTP mix	Thermo Fisher Scientific	Catalog no. F530N
MIGR1	Addgene	Catalog no. 27490
pCL-Eco	Addgene	Catalog no. 12371
Lipofectamine 3000 transfection reagent	Thermo Fisher Scientific	Catalog no. L3000015
Syringe filter, SFCA, 0.45 μm	CELLTREAT	Catalog no. 229766
Polybrene	Millipore Sigma	Catalog no. TR-1003-G
Critical commercial assays		
miRNeasy FFPE kit	Qiagen	Catalog no. 217504
The SMART-seq v4 Ultra-Low Input RNA Kit	Takara Bio	Catalog no. 634890
Agilent's high-sensitivity DNA kit	Agilent	Catalog no. 5067-4626
Nextera XT DNA library preparation kit	Illumina	Catalog no. FC-131-1024
The Qubit dsDNA HS assay kit	Thermo Fisher Scientific	Catalog no. Q32851
NovaSeq 6000 S1 reagent kit v1.5 (100 cycles)	Illumina	Catalog no. 20028319
NovaSeq 6000 SP reagent kit v1.5 (100 cycles)	Illumina	Catalog no. 20028401
Applied Biosystems High-Capacity cDNA Reverse Transcription Kit	Thermo Fisher Scientific	Catalog no. 43-688-13
TRIzol Reagent	Thermo Fisher Scientific	Catalog no. 15596018
iTaq Universal SYBR Green Supermix	Bio-Rad	Catalog no. 1725121
Mouse MCP-1 ProQuantum immunoassay kit	Invitrogen	Catalog no. A44837
Software and algorithms		
Cell Ranger	10x Genomics	
STAR	Dobin *et al.* (*96*)	
Seurat	Stuart *et al.* (*104*)	
CellChat	Jin *et al.* (*20*)	
NicheNet	Browaeys *et al.* (*34*)	
Slingshot	Street *et al.* (*46*)	
tradeSeq	Van den Berge *et al.* (*47*)	
scDblFinder	Germain *et al.* (*103*)	
DESeq2	Love *et al.* (*98*)	
Trimmomatic	Bolger *et al.* (*95*)	
RSEM	Li *et al.* (*97*)	
tximport	Soneson *et al.* (*99*)	
EnrichR	Kuleshov *et al.* (*100*)	
ShinyGO	Ge *et al.* (*101*)	
Fiji	Schindelin *et al.* (*88*)	
LabelsToROIs	Waisman *et al.* (*89*)	

Notably, *Ldha* expression, known for its higher pyruvate affinity and preference for converting pyruvate to lactate (*11*), was increased during the hypoxia phase (fig. S1C). Conversely, its isoform *Ldhb*, which favors converting lactate back to pyruvate due to its higher affinity for lactate, was down-regulated in the days immediately following the injury (fig. S1C). This suggests that SCs generate NAD^+ through pyruvate fermentation in the early days post–myotoxin-induced muscle injury. We then performed RNA sequencing on quiescent SCs (QSCs) from homeostatic muscles and the activated SCs (ASCs) from injured muscles on day 1 post-injury, a time when cytoplasmic NAD^+ is predicted to be highly produced (Fig. 1B). The transcription profiles of SCs in these two states showed segregation by principal components analysis, with the first principal component accounting for more than 90% of the variance (Fig. 1C). In addition, thousands of genes

were differentially expressed (|LogFC| > 0.5, adj. $P < 0.05$) (fig. S2A). As anticipated, genes related to hypoxia and glycolysis signaling pathways were significantly up-regulated in ASCs at 1 day post-injury (dpi) compared to QSCs (Fig. 1D), confirming the hypoxic state of these ASCs. Genes associated with the inflammatory response, particularly those involved in neutrophil chemotaxis and migration, were also highly expressed in ASCs compared to QSCs (Fig. 1E and fig. S2B). Given that neutrophils are the initial wave of immune cells to infiltrate the wounded site, peaking at day 1 post-injury (*12*), we hypothesized that ASCs may play a role in modulating neutrophil activity at the early stages of muscle regeneration.

SCs express genes associated with neutrophil attachment, adhesion, and chemoattraction

Next, we performed single-cell RNA sequencing to explore the potential interactions between SCs and neutrophils during the early hypoxic stages of muscle regeneration using mononucleated cells collected following injury at two times of the day Zeitgeber 4 (ZT4 and ZT16) from cardiotoxin-injured tibialis anterior (TA) muscles at days 1 and 3 post-injury, as well as intact uninjured muscles (Fig. 2A). Following quality control procedures, the samples were integrated into a comprehensive transcriptomic atlas comprising 58,330 cells (Fig. 2B). We then performed unsupervised clustering and, through Uniform Manifold Approximation and Projection (UMAP), identified 21 cell types annotated on the basis of the expression of established marker genes (Fig. 2B and fig. S3A) (*13*–*15*). Notably, within this atlas, two distinct clusters expressing classical neutrophil markers (S100a8 and S100a9) were delineated, termed Neutrophils_1 and Neutrophils_2 (Fig. 2B and fig. S3A). Differential gene expression analysis revealed that Neutrophils_1 are more mature than the Neutrophils_2 subtype, as evidenced by a significantly higher expression of the chemokine receptor *Cxcr2* (fig. S3B) (*16*). Correspondingly, gene ontology of biological process analysis showed that Neutrophils_1 exhibited elevated expression of genes associated with inflammatory responses (fig. S3C), signifying their pronounced inflammatory nature and advanced maturation. In contrast, Neutrophils_2 showed increased expression of genes related to lysosomal lumen acidification (fig. S3C), a characteristic of granulocyte differentiation of neutrophilic leukocyte precursors, which is essential for degradation of phagocytosed microorganisms at the inflammation sites (*17*). Intriguingly, enrichment analysis using the literature-based network in the Elsevier Pathway Collection highlighted surface expression markers regulated by myoblasts in Neutrophils_1 and by myeloblasts in Neutrophils_2, respectively (fig. S3C). This observation suggests that, like other well-established neutrophil modulators such as necrotic fibers (*18*, *19*), ASCs may contribute to the regulation of neutrophil activity, particularly influencing Neutrophils_1, following CTX injury.

On the basis of our finding that neutrophil-related genes are induced in MuSCs at day 1 post-injury (Fig. 1E), we next focused on the regulatory interplay between MuSCs and neutrophils during early muscle regeneration. To this end, we separated neutrophils and MuSCs from the total cell populations and reexamined their dynamics over time using UMAP. A few Neutrophils_1 but no Neutrophils_2 were initially presented in homeostatic muscles (day 0) (Fig. 2C). There was a marked increase in both neutrophil types on day 1 post-injury, which then sharply declined by day 3 post-injury (Fig. 2C). Potential cross-communication between MuSCs and the two neutrophil types were delineated using CellChat, which can infer intercellular signaling network based on single-cell RNA sequencing data (*20*). This was illustrated through vectorial circle plots representing interactions between any two cell groups (Fig. 2D). The communicative links mediated by MuSCs were most prominent on day 1 post-injury, highlighted by the densest edge weights directed from MuSCs toward the neutrophil populations (Fig. 2D). The nature of MuSC-initiated interactions evolved across the different days. Interactions involving laminin and collagen signaling, which facilitate cell attachment or adhesion, along with α chemokines featuring the CXC motif (CXCL) secreted by MuSCs, were prevalent at all observed time points. In contrast, β chemokines with the CC motif (CCL) were exclusively secreted by ASCs at 1 dpi, playing a crucial role in mediating MuSC communication with both neutrophil types (Fig. 2E).

NAD^+ boosts chemokine gene expression and neutrophil recruitment in regeneration

CXCL and CCL chemokines are potent neutrophil chemoattractants (*21*). Given that hypoxia is known to modulate chemokine and chemokine receptor expression (*22*, *23*), we investigated whether low oxygen tension or, more specifically, anaerobically regenerated NAD^+, could trigger chemokine gene expression in SCs. First, we cultured wild-type myoblasts under normoxia or hypoxia (1% O_2) for short durations ranging from 1 to 6 hours and measured NAD^+ levels by high-performance liquid chromatography. Our results showed a clear, duration-dependent increase in total NAD^+ levels in myoblasts exposed to hypoxia compared to those cultured under normoxia (Fig. 3A). To uncouple NAD^+ redox cycling from hypoxia, we expressed cytosolic NADH oxidase from *L. brevis* (*LbNOX*) in myoblasts (fig. S4, A and B), which allows for a compartment-specific elevation of the NAD^+/NADH ratio (*24*). Primary myoblasts from *cytoLbNOX*$^{LSL/LSL}$ mice were isolated and treated with Cre-expressing or control adenovirus (Fig. 3B). *CytoLbNOX*-expressing myoblasts exhibited a significant increase in intracellular NAD^+ (fig. S4C), a decrease in NADH levels (fig. S4D), resulting in increased NAD^+/NADH ratio (fig. S4E). Seventy-two hours post infection, the cells were exposed to normoxic (21% O_2) or hypoxic (1% O_2) conditions for 24 hours. Among the candidate neutrophil chemotaxis–related genes identified as significantly up-regulated in 1-dpi ASCs compared to QSCs (fig. S2B), *Ccl2* was notably the only chemokine that could be induced not only by hypoxia but also by cytoLbNOX, even under normoxia (Fig. 3C and fig. S5). A two-way analysis of variance (ANOVA) revealed a significant interaction effect between oxygen concentration and cytoLbNOX-mediated NAD^+ regeneration ($P = 0.008$). Hypoxia treatment did not further increase gene expression in cytoLbNOX-expressing myoblasts (Fig. 3C), suggesting that hypoxia may induce *Ccl2* expression via NAD^+ regeneration. Consistent with this observation, the addition of galloflavin, a lactate dehydrogenase inhibitor that impedes NAD^+ regeneration (*25*), diminished *Ccl2* expression under hypoxia conditions (Fig. 3D) but failed to inhibit its up-regulation in cytoLbNOX-expressing myoblasts (Fig. 3E), further supporting the pivotal role of NAD^+ regeneration, rather than lactate, in this context.

Considering the chemoattractant properties of CCL2, we examined whether *cytoLbNOX*-driven NAD^+ augmentation could enhance neutrophil recruitment within regenerating muscles in vivo. To this end, we crossed *cytoLbNOX*$^{LSL/LSL}$ mice with a line expressing Cre recombinase under the control of a tamoxifen-inducible *Pax7* promoter, resulting in excision of an upstream STOP codon to allow for muscle stem cell–specific *cytoLbNOX* expression (*LbNOX*^{musc}).

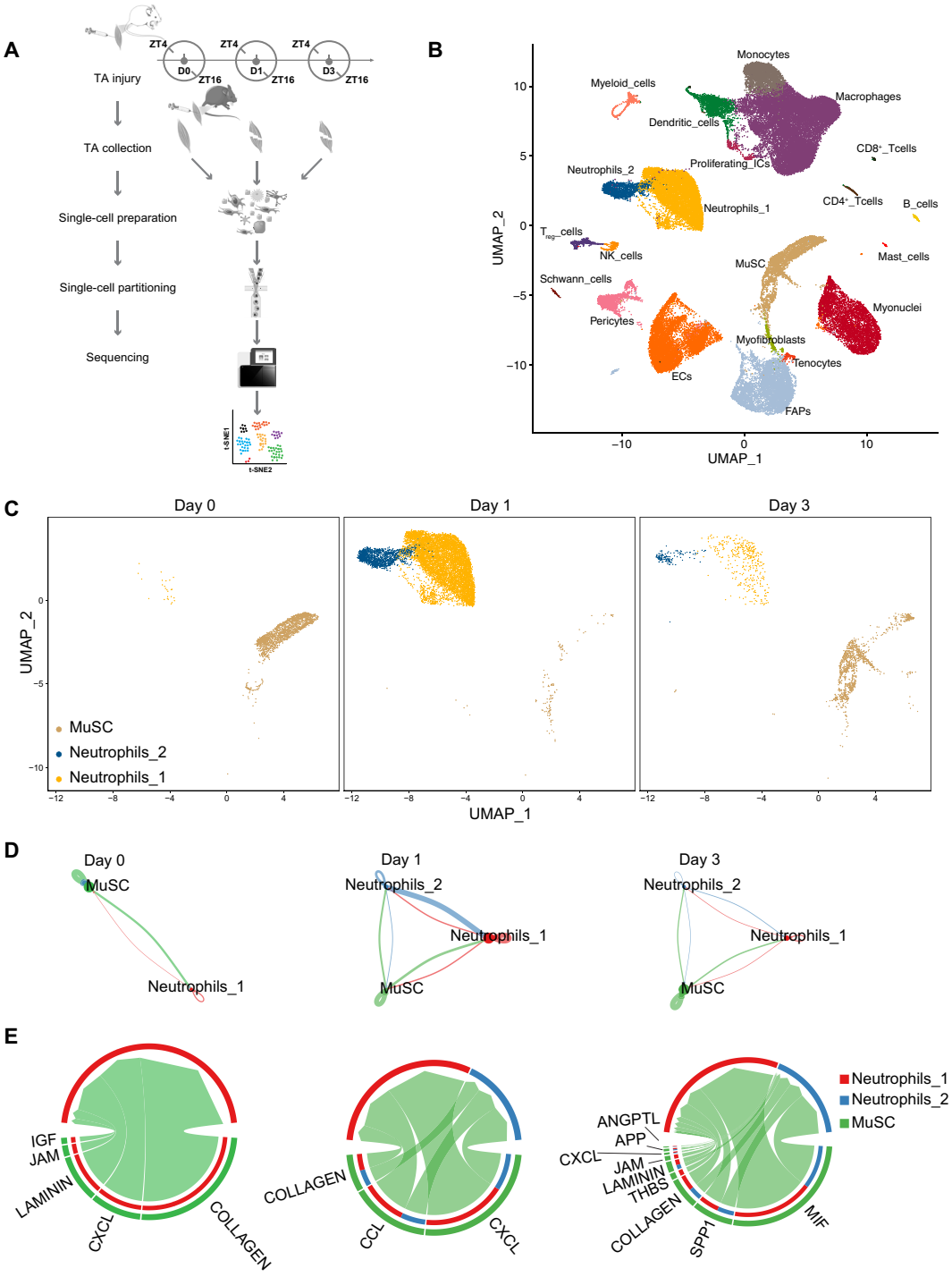

Fig. 2. Interactions between SCs and neutrophils during early muscle regeneration. (**A**) Schematic diagram of single-cell sequencing experiment using mononucleated cells from the TA muscles of both hindlimbs were collected at ZT4 and ZT16 on day 0, 1, and 3 after injury. Single cells were collected through fluorescence-activated cell sorting (FACS), excluding dead cells identified by propidium iodide (PI) staining. Samples from each time point and day were captured in droplet emulsions using a 10x Chromium Controller (10x Genomics), aiming for 10,000 cells per sample, and then sequenced. (**B**) UMAP visualization of 21 annotated cell types within pooled TA muscle cells from all six samples. EC, endothelial cells; FAPs, fibro-adipogenic progenitors. (**C**) UMAP of neutrophil and MuSC single-cell transcriptomes split by days post-injury. (**D**) Chord diagram showing the specific ligand-receptor or signaling pathway–mediated interactions among the three cell clusters. The edge colors correspond to the source (sender) of the signal, and edge weights are proportional to the interaction strength, with thicker lines indicating stronger signals. Circle sizes reflect the number of cells in each cell group. (**E**) Circle plot showing the aggregated cell-cell communication network sent from MuSCs and received by individual clusters of neutrophils at various days post-injury. The inner, thinner bar colors represent the targets receiving signals from the corresponding outer bars. The size of the inner bar is proportional to the signal strength received by the targets.

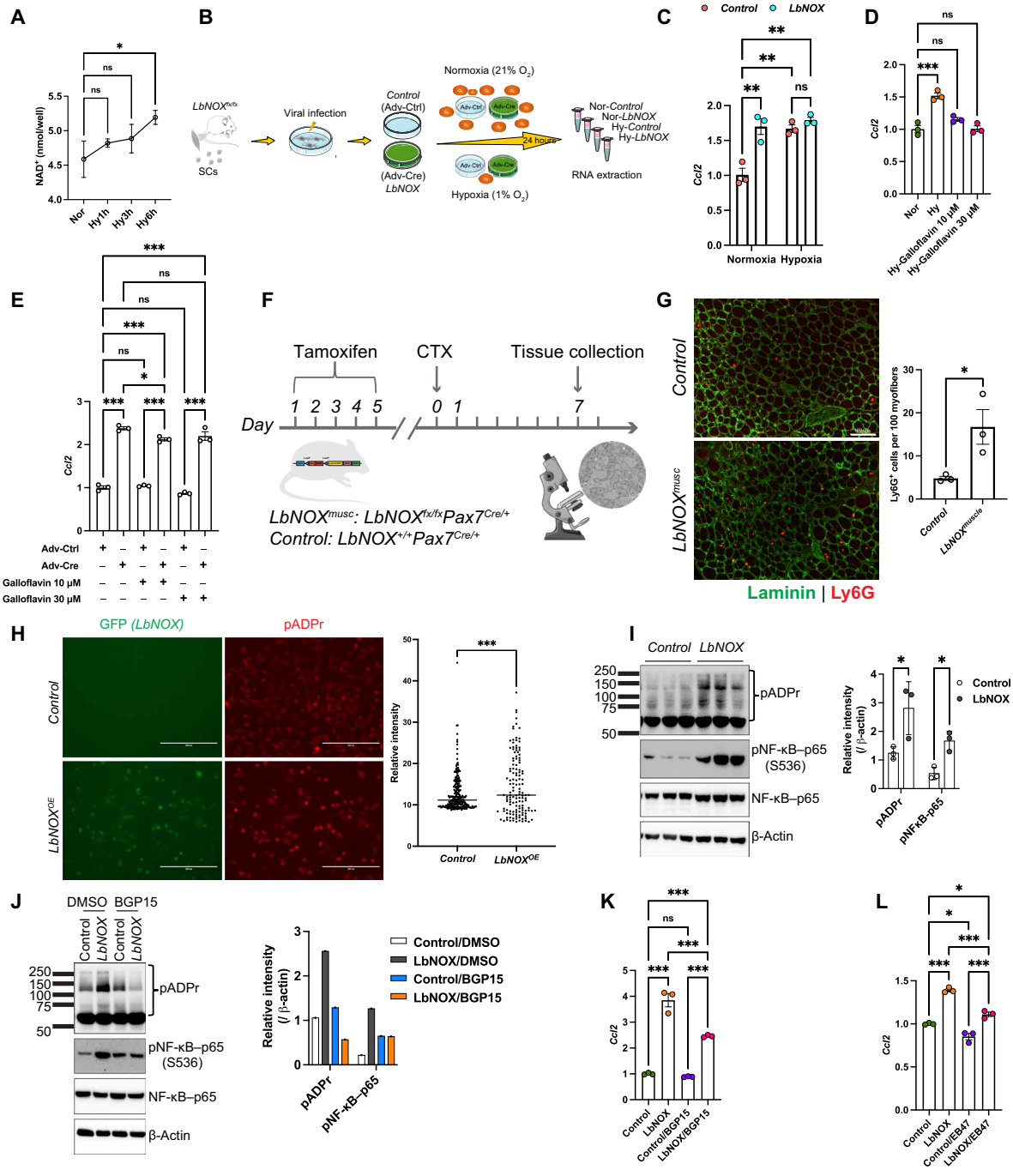

Fig. 3. NAD^+ regeneration-induced immunomodulatory gene expression via PARP-mediated PARylation and NF-κB activation. (**A**) NAD^+ contents in wild-type myoblasts cultured in normoxia and hypoxia up to for 6 hours. $n = 3$ wells per condition. $^*P < 0.05$ by one-way analysis of variance (ANOVA) test. (**B**) Schematic diagram of viral induction of LbNOX expression in primary myoblasts. (**C**) *Ccl2* expression in myoblasts under conditions described in (B). $^*P < 0.05$, $^{**}P < 0.01$ by two-Way ANOVA. ns, nonsignificant. (**D**) *Ccl2* expression in myoblasts subjected to hypoxia (1% O_2) for 24 hours, both in the absence and presence of galloflavin. Normoxic myoblasts (21% O_2) served as controls. $^{***}P < 0.001$ by one-way ANOVA, comparing each group to normoxic myoblasts. (**E**) *Ccl2* expression in myoblasts treated for 24 hours with or without galloflavin. $^*P < 0.05$, $^{***}P < 0.001$ by two-way ANOVA analysis. (**F**) Schematic diagram of MuSC conditional *LbNOX* (*LbNOX*^{musc}) mouse experiment ($n = 3$ per group). (**G**) Immunohistochemistry and quantification of mouse TA muscle for $Ly6G^+$ neutrophils and laminin. Scale bar, 100 μm. (**H**) Representative immunofluorescence image and quantification of neutrophils in mouse TA muscle under conditions described in (F). $^*P < 0.05$ by unpaired Student's *t* test. (**I**) Immunofluorescence of global PARylation in myoblasts. *LbNOX* expression is marked by GFP coexpression. Scale bar, 200 μm. $^*P < 0.001$ by unpaired Student's *t* test. (**J**) Immunoblot analysis and quantification of global PARylation, serine-536–phosphorylated and total NF-κB p65 subunit, and β-actin in the absence (I) or presence (J) of BGP15. $^*P < 0.05$ by unpaired Student's *t* test. DMSO, dimethyl sulfoxide. (**K**) Immunomodulatory gene expression following a 6-hour treatment with or without BGP15. $^{***}P < 0.001$ by two-way ANOVA. (**L**) *Ccl2* expression following a 6-hour treatment with or without EB47. $^*P < 0.05$, $^{***}P < 0.001$ by one-way ANOVA.

One week following tamoxifen induction, we performed cardiotoxin-induced TA muscle injury and assessed neutrophil presence in both uninjured muscles and at 7 dpi via Ly6G immunohistochemistry (Fig. 3F and fig. S6). Little or no Ly6G-positive signal was detected in the homeostatic uninjured muscles of both groups (fig. S6). At 7 dpi, neutrophil numbers in control muscles had largely diminished, whereas *LbNOX*^{musc} mice retained significantly more neutrophils (Fig. 3G), aligning with our hypothesis that cytoplasmic NAD^+ mediates neutrophil activity in regenerating muscle.

NAD^+ serves as a critical cosubstrate for two main families of post-translational modification enzymes: the ADP-ribosyltransferase (ARTs) and the SIRTs (*26*–*28*). Given that PARP enzymes, a subset of ARTs, can activate the major immunoregulatory transcription factor NF-κB (*29*), we asked whether cytoplasmic NAD^+ might regulate chemokines expression via PARP-mediated poly-ADP ribosylation (PARylation). *CytoLbNOX*-expressing myoblasts showed increased PARylation and NF-κB activation (Fig. 3, H and I), which we also observed in hypoxia (fig. S7A). Notably, treatment with BGP15, a broad PARP inhibitor (*30*), reduced intracellular protein PARylation and NF-κB activation (Fig. 3J), leading to a significant decrease in *Ccl2* expression in *cytoLbNOX*-expressing myoblasts (Fig. 3K). This implies that PARP-mediated PARylation contributes to NAD^+-mediated *Ccl2* expression via NF-κB. We found that *Parp1* was significantly increased ($\log_2$FC = 1.68, adj. $P = 1.14 \times 10^{-22}$) in 1-dpi ASCs compared to QSCs, while other *Parp* mRNAs were decreased (fig. S7B). This is consistent with previously published transcriptomic data from MuSCs following cardiotoxin injury, which found a peak of *Parp1* expression at 2 dpi (fig. S7C) (*9*). The PARP1-specific inhibitor EB47 (*31*), like BGP15, significantly suppressed *Ccl2* expression in *cytoLbNOX*-overexpressing myoblasts but not in control cells (Fig. 3L). Together, these data indicate that PARP1 may mediate NAD^+-dependent neutrophil signaling and *Ccl2* expression in ASCs.

Hypoxic regulation of immunomodulatory gene expression is under circadian control

Given the established role of the SC circadian clock in regulating hypoxic NAD^+ regeneration in myoblasts and muscle repair capacity following $_{injury}$ (*4*), we hypothesized that NAD^+-induced immunomodulatory gene expression might also be under circadian control. In support of this, total RNA sequencing of wild-type and *Bmal1*$^{-/-}$ primary myoblasts exposed to acute hypoxia (6 hours, 1% O_2) (fig. S8A) revealed a marked down-regulation of chemokine signaling pathway–related genes (fig. S8, B and C). Previously, we demonstrated in cultured myoblasts that *Bmal1*-deficent myoblasts exhibit a reduction in hypoxic growth and myogenic capacity, which can be partially rescued by *cytoLbNOX*-expression (*4*). Building upon these findings, we investigated the effect of *cytoLbNOX* expression in rescuing the muscle regeneration defects of SC-specific *Bmal1* knockout (*Bmal1*^{musc}) mice in vivo (fig. S8D). While *cytoLbNOX* expression partially restored the regenerative defects of *Bmal1*^{musc} mice in terms of fiber size, the overall muscle integrity in *cytoLbNOX*-expressing mice was worsened compared to control mice (fig. S8, E and F). This may be attributed to the cyto*LbNOX*-induced neutrophil activation mechanism described in this study, as we observed a pronounced presence of mononucleated cells in the muscles of *cytoLbNOX*-expressing mice at day 7 post-injury (fig. S8E).

Next, we performed cardiotoxin-induced injuries in TA muscles at ZT4 and ZT16, corresponding to periods of low and high BMAL1 activity, respectively (*4*, *32*). ASCs were isolated at 24 hours (1 day) post-injury (Fig. 4A) and subjected to total mRNA sequencing (Fig. 4B). Aligning with our previous findings that the HIF signaling pathway is modulated by circadian clock (*4*, *33*), genes related to the hypoxia response were significantly more up-regulated in ASCs from muscles injured at ZT16 than at ZT4 (Fig. 4C). Notably, among the genes specifically induced in ASCs following injury at ZT16 versus ZT4 were those associated with inflammatory response, particularly neutrophil chemotaxis and chemokine-mediated signaling pathways (Fig. 4C). These TOD-dependent differences were not observed in homeostatic QSCs at both ZT4 and ZT16, suggesting that they arise following injury (fig. S9).

Our mononucleated muscle cell samples for single-cell RNA sequencing described earlier were collected at both ZT4 and ZT16 from both homeostatic TA muscles and those injured at ZT4 and ZT16 on 1 and 3 dpi (Fig. 2A). Reexamining the TOD-dependent dynamics within the UMAP encompassing neutrophils and MuSCs (Fig. 4D), we used NicheNet (*34*) to dissect TOD-dependent communication differences between MuSCs and neutrophils, designating MuSCs as the signal "sender" and neutrophils as the "receiver." According to NicheNet's guidelines, a Pearson correlation coefficient score around 0.10 or higher indicates statistically significant ligand-mediated cross-talk. Our results showed more substantial ligand-mediated interactions between MuSCs and the Neutrophils_1 population on day 1 post-injury, while interactions with Neutrophils_2 did not achieve a high Pearson score (Fig. 4E). The differences in these interactions were not directly tied to cell proportion differences, as the Neutrophils_1 proportion remained similar between time points (35.2% at ZT16 versus 37.6% at ZT4) (fig. S10A). In contrast, although the Neutrophils_2 population was nearly twice as large at ZT4 compared to ZT16 (9.9% at ZT4 versus 4.6% at ZT16) (fig. S10A), the ligand-mediated interactions with MuSCs were weaker, suggesting that the observed differences in cell-cell communication were driven by factors beyond cell number differences. *Ccl2* emerged as the sole CCL-type chemokine among the top ligands, exhibiting high activity in inducing target gene expression in Neutrophils_1 (Fig. 4E and fig. S10, B and C). Furthermore, *Ccl2* gene expression was notably higher in ASCs at ZT16 compared to ZT4 on 1 dpi (Fig. 4F and fig. S2B).

We next investigated whether the PARP1-mediated mechanism contributes to the TOD-dependent changes in *Ccl2* expression levels. To address this question, we used an in vitro synchronization approach, a well-established model for studying the self-sustaining properties of circadian rhythms (*35*–*38*). Primary myoblasts were synchronized with dexamethasone (1 μM for 1 hour) to align their internal circadian clocks and then exposed to hypoxia to simulate the conditions that ASCs experience on the first dpi (Fig. 4G). Cells were harvested every 4 hours to measure *Ccl2* expression over the 24-hour circadian cycle. Our quantitative polymerase chain reaction (qPCR) data revealed a clear circadian oscillation of *Ccl2*, mirroring the expression pattern of *Bmal1*, with *Ccl2* expression being low at circadian time 4 (CT4) and high at CT16 (Fig. 4H). We then assessed NF-κB activation in synchronized myoblasts at CT4 and CT16 under hypoxia, in the presence and absence of the PARP1 inhibitor EB47, via Western blot analysis. NF-κB activity, indicated by an increase in phosphorylation of the NF-κB p65 subunit at serine-536, was higher in synchronized myoblasts at CT16, a time point that correlated with elevated *Bmal1* expression levels (Fig. 4H), compared to CT4 under hypoxia (Fig. 4I). Following treatment with EB47 for 6 hours, we observed reduced NF-κB p65 phosphorylation at serine-536 in synchronized myoblasts at CT16 but not at CT4

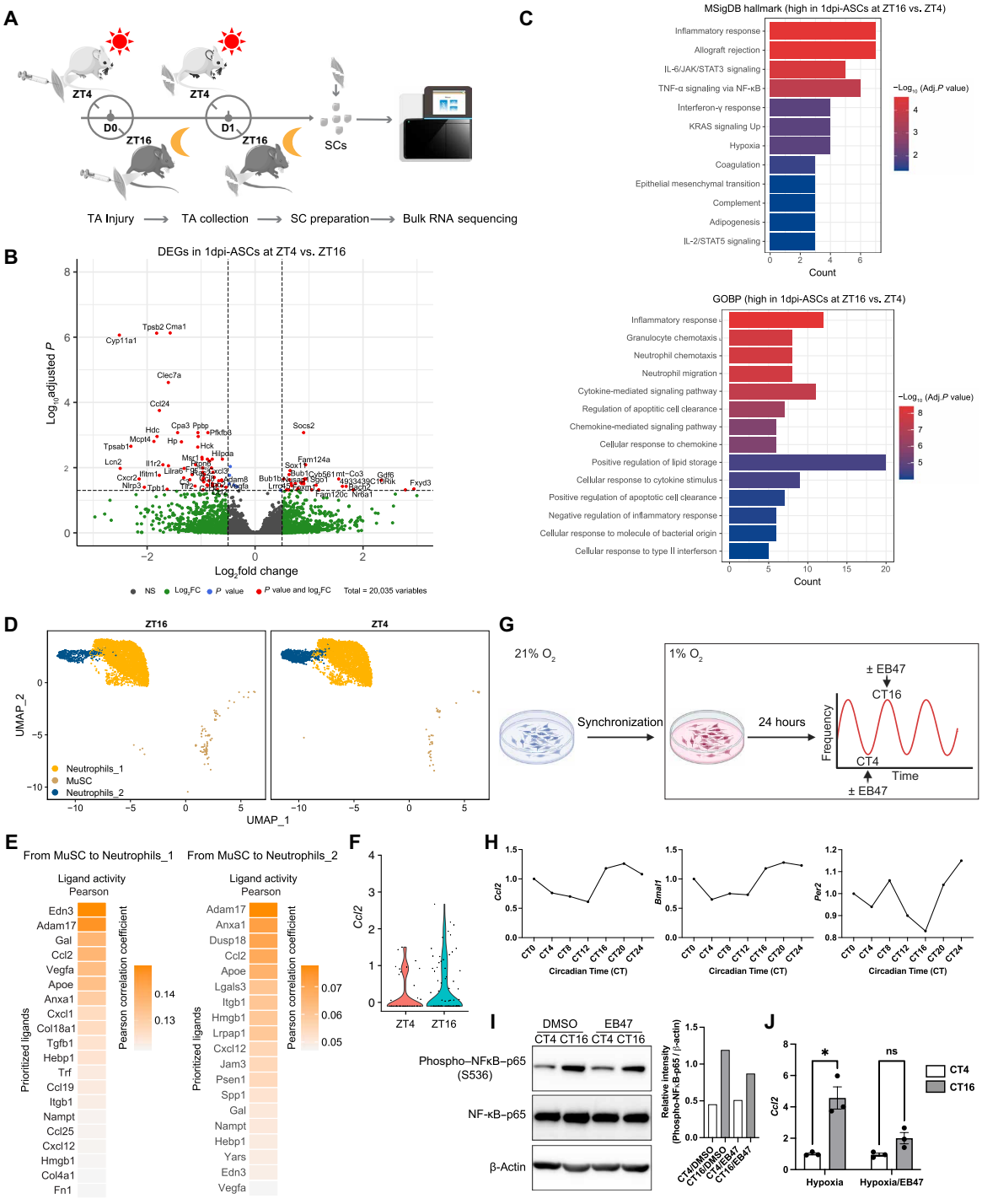

Fig. 4. TOD-dependent immunomodulatory expression in ASCs at day 1 post-injury. (**A**) Schematic diagram of cardiotoxin-induced injury and SC isolation experiments in Pax7-zsgreen mice. (**B**) Volcano plot showing differentially expressed genes (DEGs, adjusted $P < 0.05$) in ASCs harvested from injured TA muscles at ZT4 compared to ZT16 at day 1 post-injury. (**C**) Signaling pathway enrichment analysis for genes more highly expressed in ASCs at ZT16 compared to ZT4 at 1 dpi. (**D**) UMAP of neutrophil and MuSC single-cell transcriptomes split by the TOD on day 1 post-injury. (**E**) Heatmap of ligand activities by NicheNet analysis showing ranked potential ligands expressed in the signal sender (MuSCs) that could predict the observed DEGs in neutrophil populations between ZT4 and ZT16 on day 1 post-injury. (**F**) Violin plot comparing expression of *Ccl2* in ASCs at ZT4 and ZT16 on day 1 post-injury. (**G**) Schematic diagram of myoblast synchronization experiment. (**H**) Expression of *Ccl2*, *Bmal1*, and *Per2* over the 24-hour cycle in dexamethasone-synchronized myoblasts under hypoxia. (**I**) Immunoblot analysis and relative quantification of total and serine-536–phosphorylated NF-κB p65 subunit and β-actin in synchronized myoblasts under hypoxia at CT4 and CT16, following a 6-hour treatment with or without EB47. (**J**) *Ccl2* expression in synchronized myoblasts under hypoxia at CT4 and CT16, following a 6-hour treatment with or without EB47. *$P < 0.05$ by two-way ANOVA analysis. ns, nonsignificant.

(Fig. 4I). While hypoxia-induced *Ccl2* expression was significantly higher at CT16 compared to CT4, treatment with EB47 abolished this difference (Fig. 4J).

Ccl2 expression is associated with TOD-dependent differences in SC proliferation

A previous study demonstrated that conditioned medium from neutrophil cultures can promote myoblast proliferation while suppressing their differentiation (*39*). This prompted us to investigate whether the TOD-dependent interactions between MuSCs and neutrophils might reciprocally influence SC fate decisions during muscle regeneration. To explore this, we analyzed the cellular heterogeneity within the MuSC populations from our single cell–transcriptomic atlas. Unsupervised clustering identified seven distinct subpopulations of myogenic cells (Fig. 5A). Notably, cells in cluster 3 exhibited high expression of *Pax7* and genes like *Spry1*, *Cd34*, *Cdkn1b*, and *Pdk4*, which are recognized markers of deep QSCs (dQSCs) (*40*–*42*). Further classification of the clusters was based on gene sets indicative of early commitment (e.g., *Myf5*, *Egr2*, *Egr3*, *Myc*, *Jund*, *Dnajb1*, *Ccl8*) (*41*, *42*), activation/proliferation (*Myod1*, *Mki67*, *Cdk1*, *Ccnb1*) (*43*), differentiation (*Myog*, *Myl4*) (*7*, *44*), and self-renewal (*Cdk6*, *Ccnd1*, *Tgfbr3*, *Smad4*) (*45*), leading to their designation as primed QSC 1 and 2, committed SCs, dividing SCs, differentiating SCs, and renewing SCs (Fig. 5A and fig. S11A). A temporal analysis on UMAP highlighted that QSCs and some committed SCs were prevalent in homeostatic muscles, whereas dividing and differentiating SCs were mainly observed in regenerating muscles by 3 dpi (fig. S11B).

To better understand the hierarchical organization and validate the classification of these myogenic subclusters, we applied Slingshot (*46*), a single-cell trajectory inference analysis, to the entire myogenic cell population within the atlas. This analysis delineated a sequential trajectory from deep quiescence through primed quiescence and commitment/activation, leading to division, which then bifurcated toward self-renewal (lineage 1) or differentiation (lineage 2) (Fig. 5B). Along this pseudotime trajectory, *Pax7* expression gradually decreased, while *Myod1* expression increased in both lineages (fig. S11C). In the self-renewal lineage, *Myog* expression spiked before sharply decreasing, whereas in the differentiation lineage, *Myog* expression steadily rose (fig. S11C).

To elucidate differential gene expression patterns between ZT4 and ZT16 within each myogenic lineage, we used the "conditionTest" function from the tradeSeq package (*47*). This analysis revealed 88 genes with significant differential expression (adjusted P value < 0.05, fold change > 1) across pseudotime (Fig. 5C). Subsequent KEGG pathway enrichment analysis linked these genes predominantly to the cell cycle (Fig. 5D). We further assessed the expression trajectories of two key cell division markers, cyclin-dependent kinase 1 (*Cdk1*) and *Mki67*, over pseudotime at both ZT4 and ZT16. Notably, while there was an initial surge in the expression of both regulators at lower pseudotime values within the differentiation lineage (lineage 2) of ZT4 myogenic cells, but not in ZT16 cells, this increase appeared to be driven by a single cell (Fig. 5E). Overall, however, the expression levels of *Cdk1* and *Mki67* in ZT16 cells within this lineage rose more rapidly than in ZT4 cells, eventually reaching comparably high levels at later pseudotime stages (Fig. 5E).

The expression dynamics we observed suggest a potential regulatory effect of the TOD on key cell cycle regulators, which may in turn influence the proliferation trajectory of SCs after activation. To investigate this influence, we induced injury in TA muscles at ZT4 and ZT16 and then quantified the frequency of SCs in the total muscle cell population by day 3 post-injury, a peak time for dividing myonuclei (*48*), using *Pax7*-zsgreen reporter mice (*49*). Flow cytometry analysis revealed a significantly higher frequency of zsgreen$^+$ SCs in TA muscles injured at ZT16 compared to those injured at ZT4 at 3 dpi (Fig. 5F). However, no difference in the frequency of zsgreen$^+$ SCs was observed in homeostatic TA muscles between ZT4 (1.005% ± 0.26) and ZT16 (1.128% ± 0.32).

To determine the extent to which SC-expressed CCL2 contributes SC proliferation, we transduced freshly isolated SCs with a *Ccl2*-expressing retrovirus and transplanted them into TA muscles of wild-type C57BL/6 mice 6 hours following cardiotoxin injury (Fig. 5G). The contralateral TA muscles were subjected to the same preinjury but received control virus (R1)–transduced SCs. The transplanted myogenic progenitors, labeled by green fluorescent protein (GFP) carried by the viral vector, allowed for the tracking of GFP$^+$-SCs within the total SCs population, characterized as VcamI$^+$Scal1$^-$CD31$^-$CD45$^-$ (*50*), at 3 dpi (Fig. 5G). Before this experiment, we first verified the role of CCL2 as a secreted chemokine by comparing its levels in culture media from myoblasts infected with either *Ccl2*-expressing or control retroviruses using enzyme-linked immunosorbent assay (ELISA) (Fig. 5H). Notably, we observed a significantly higher frequency of *Ccl2*-overexpressing SCs in the TA muscles of recipient mice compared to those transplanted with control virus-infected SCs (Fig. 5I). This increase likely resulted from the CCL2 released into the niche by the exogenous SCs, which was also reflected in an increase in the total MuSC population compared to muscles receiving control virus-infected SCs (Fig. 5I).

Neutrophil depletion diminishes TOD effects on SC and muscle regeneration

Our previous studies, along with others, showed a TOD-dependent variation in skeletal muscle repair following cardiotoxin-induced injury, with more effective regeneration occurring during active phase compared to the rest phase (*4*, *5*). The enduring impact of this TOD effect remains underexplored. To investigate whether the difference is transient or has long-lasting consequences, we induced TA muscle injuries with cardiotoxin at ZT4 or ZT16, repeating the process three times at 30-day intervals (Fig. 6A). Histological examination conducted 30 days after the last injury revealed that TA muscles subjected to repeated injuries at ZT4, corresponding to a period of lower BMAL1 activity, exhibited a higher proportion of small regenerated myofibers and lower proportion of large myofibers compared to those injured at ZT16 (Fig. 6, B and C). In addition, we assessed muscle strength by measuring torque under continuous electronic stimuli at multiple frequencies at the corresponding time of injuries (Fig. 6D). As has been previously reported, max tetanic force production in the uninjured TA muscle exhibited variations depending on the TOD, with increased peak force during tetanic contractions (Max tetanic) observed in the early rest phase (ZT4) compared to the active phase (ZT16) (Fig. 6E) (*51*–*55*). We also assessed recovery of muscles following repeated injuries at either ZT4 or ZT16 by comparing the Max tetanic of injured muscles to that of uninjured ones at identical times of day. While the interaction between TOD and injury status did not reach significance by two-way ANOVA, we observed a trend toward reduced recovery in mice injured at ZT4, as compared to ZT16 (Fig. 6E). These findings point toward a potential lasting influence of TOD on muscle health and regeneration.

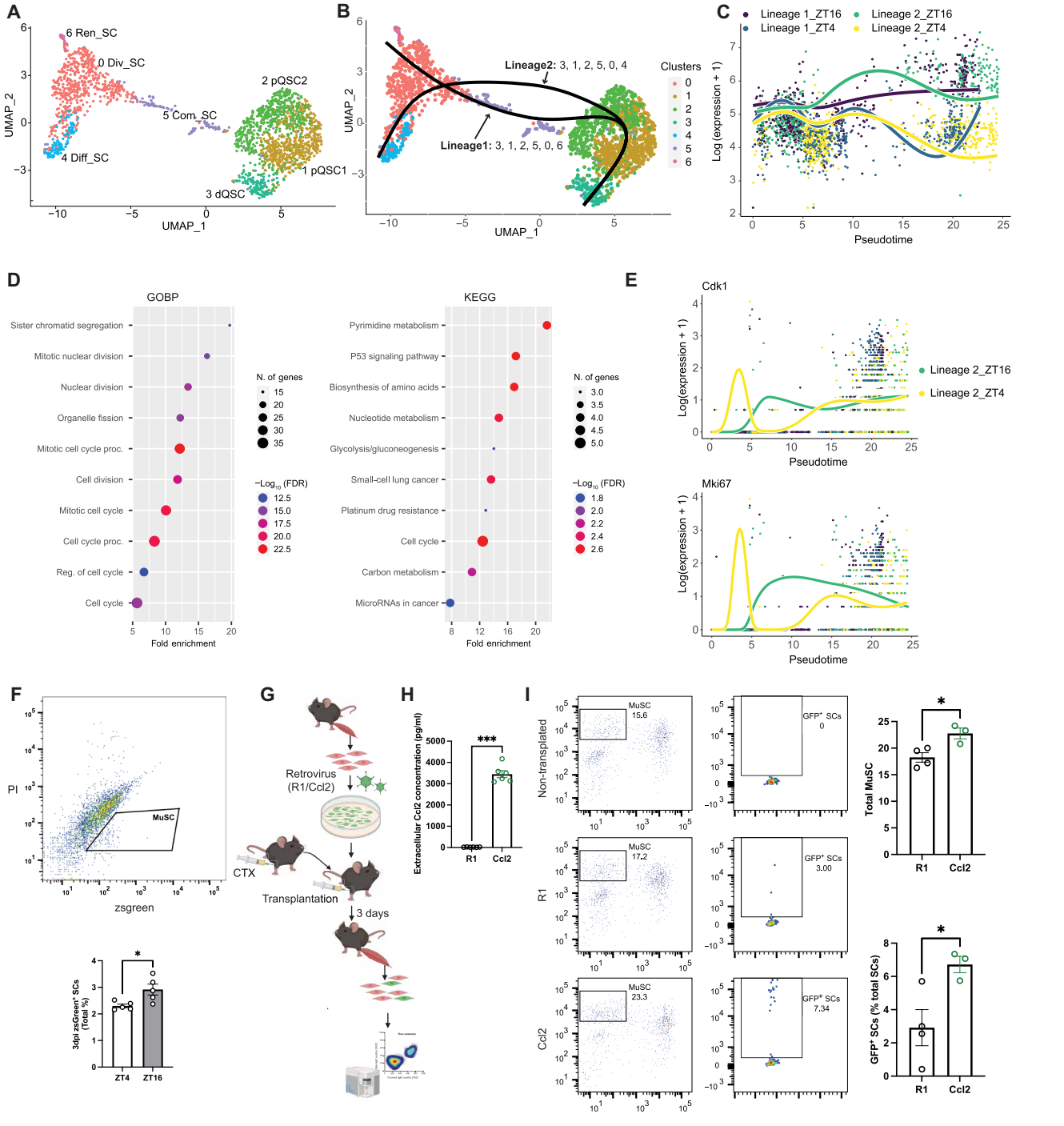

Fig. 5. Ccl2 secretion by SCs promotes TOD-dependent proliferative differences. (**A**) UMAP visualization of the subclustered MuSC populations, with subclusters defined as dQSC, primed quiescent SCs (pQSC). committed SCs (Com_SC), dividing SCs (Div_SC), differentiating SCs (Diff_SC), and renewing SCs (Ren_SC). (**B**) Pseudotime trajectory inference analysis of MuSC subclusters by Slingshot, with deep QSCs serving as the starting point of pseudotime. (**C**) Pseudotime ordered single-cell expression trajectories for the genes that were most differentially expressed between the time points of ZT4 and ZT16 in lineage 1 and 2. (**D**) Signaling pathway enrichment analyses on the DEGs from (C). (**E**) Pseudotime ordered single-cell expression trajectories for the cell cycle regulators Cdk1 and Mki67 at ZT4 and ZT16 within lineage 2. (**F**) Representative FACS plot for MuSC gating (zsGreen$^+$) at 3 dpi (top) and quantification of MuSC frequency within total mononucleated muscle cells (bottom). *$P < 0.05$ by unpaired Student's *t* test ($n = 5$ mice per time point). (**G**) Schematic diagram of experiment using wild-type mice transplanted with myoblasts expressing GFP$^+$ retrovirus and either *Ccl2* (*Ccl2*-virus) or a control (R1) retroviruses ($n = 4$). Cardiotoxin-induced TA muscle injuries were performed at ZT16. Transplantation of 10^5 SCs occurred at 6 hours post-injury. At day 3 post-transplantation, total MuSC frequency and the percentage of GFP$^+$ SCs within the total MuSC population were assessed by flow cytometry. (**H**) Quantification of CCL2 by ELISA in the media after 24 hours of culture from equal number of myoblasts infected with either *Ccl2*-expressing or control retrovirus. (**I**) Quantification of total MuSCs and GFP$^+$ MuSCs in recipient TA muscles as described in (G). *$P < 0.05$ by unpaired Student's *t* test.

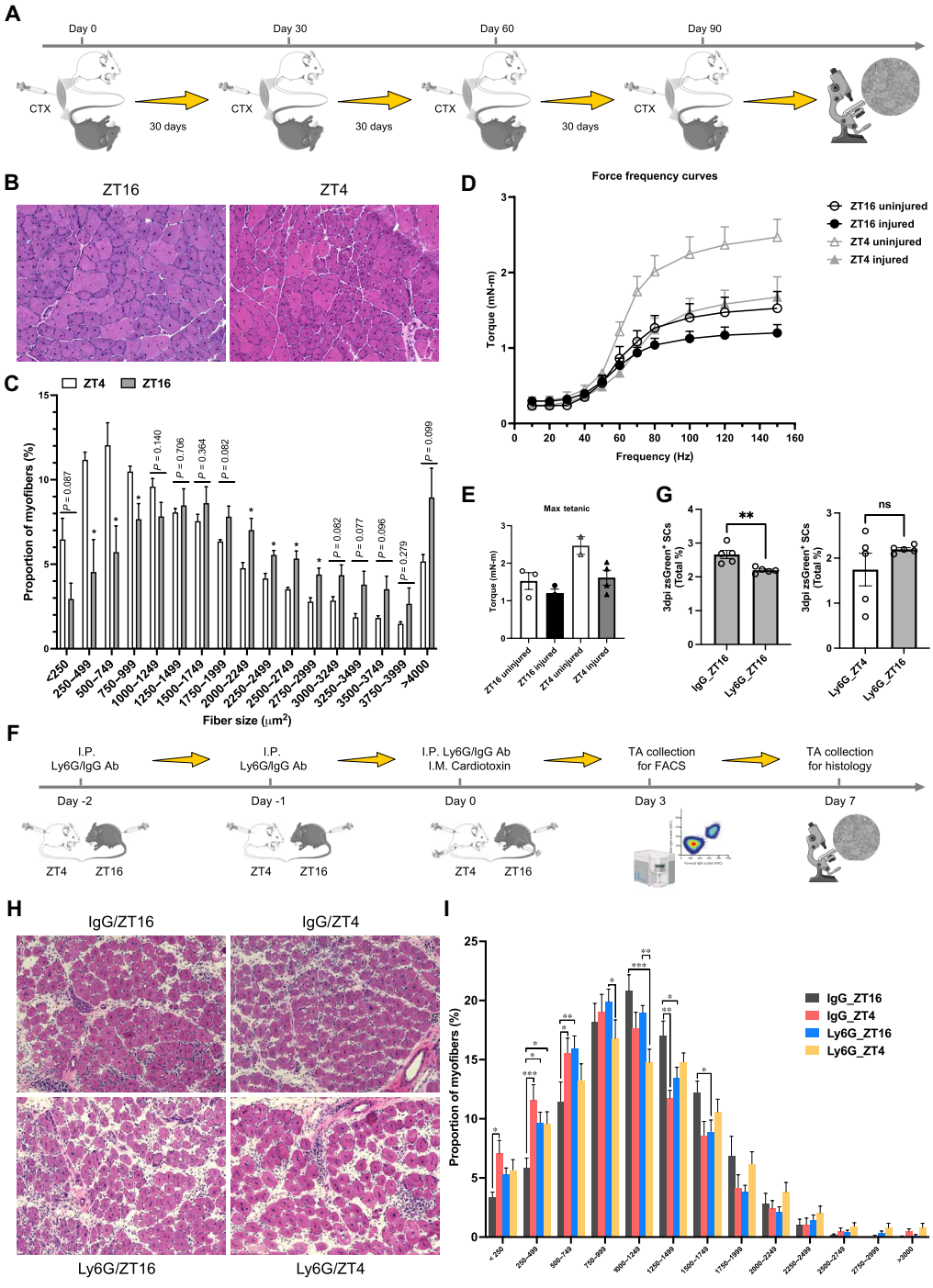

Fig. 6. Reduction of TOD-dependent variations in SC proliferation and muscle regeneration through neutrophil depletion. (**A**) Schematic diagram of repeated cardiotoxin-induced injury at different times of day in wild-type mice ($n = 3$ per time point). Mice were euthanized at 30 days post-final injury, and TA muscles were assessed for muscle remodeling and function. (**B**) Representative hematoxylin and eosin (H&E) staining and (**C**) quantification of myofiber size distribution of the repeatedly injured TA muscles at ZT16 and ZT4 described in (A). (**D**) Measurement of torque variations in response to different stimulation frequencies in the TA muscles that were repeatedly injured at ZT4 and ZT16. Torque at each frequency along the force frequency curve plotted as mean ± SEM. (**E**) Peak torque generated in the force frequency curve (mean; SEM) for each group: ZT16u (1.526; 0.2237), ZT16i (1.200; 0.1101), ZT4u (2.470; 0.2365), ZT4i (1.614; 0.1968). (**F**) Schematic diagram of Pax7-zsGreen mice following transient neutrophil depletion through three consecutive intraperitoneal injections of Ly6G antibody ($n = 5$ per group). Control mice received IgG antibody injections from the same host species as the Ly6G antibody. (**G**) Quantification of zsGreen$^+$ SCs on 3 dpi in the injured TA muscles from both IgG and Ly6G-treated mice (top), and in TA muscles from neutrophil-depleted mice injured at ZT4 and ZT16 (bottom). $^{**}P < 0.01$ by unpaired Student's t test. ns, nonsignificant. (**H**) Representative H&E staining of TA muscles from IgG and Ly6G treated mice that were injured at ZT4 and ZT16. (**I**) Quantification of myofiber size distribution in the injured TA muscles shown in (H). $^{*}P < 0.05$, $^{**}P < 0.01$, $^{***}P < 0.001$ by two-way ANOVA test.

To further probe the role of neutrophils in mediating the TOD effect on muscle regeneration, we depleted neutrophils in the early stages post-injury. Depletion was achieved through three successive intraperitoneal injections of a Ly6G antibody. On the day of the final injection, we induced TA muscle injuries with cardiotoxin and examined neutrophil infiltration 18 hours later (fig. S12A). Flow cytometry analysis confirmed that the Ly6G antibody specifically reduced neutrophil infiltration compared to the control immunoglobulin G (IgG) antibody, with minimal impact on other immune cells like monocytes (fig. S12B). Leveraging this neutrophil depletion strategy, we evaluated its effect on SC proliferation at 3 dpi and on muscle regeneration at 7 dpi, following cardiotoxin-induced injuries at ZT4 and ZT16 (Fig. 6F). Flow cytometry–based cell quantification showed that neutrophil depletion reduced the frequency of SCs in TA muscles injured at ZT16 compared to those treated with control IgG antibody (Fig. 6G, left). The TOD-dependent disparities in SC proliferation at 3 dpi are much less prominent in the absence of neutrophils (Fig. 6G, right) and in muscle regeneration at 7 dpi (Fig. 6, H and I), suggesting that neutrophils are key modulators of the TOD effect in muscle repair processes.

Together, our study supports a model whereby hypoxic cytosolic NAD^+ regeneration following muscle injury bolsters cell proliferation and concurrently modulates proinflammatory signaling, as induced by the activation of PARP1 and NF-κB pathways. This process is crucial for the chemotactic recruitment of neutrophils and their interaction with MuSCs, facilitating stem cell activation and proliferation. The circadian clock further influences this process by fine-tuning the hypoxia-induced anaerobic NAD^+ regeneration, imparting TOD-dependent differences in muscle repair efficacy (Fig. 7).

DISCUSSION

Metabolic processes are essential for biological functions, with glycolysis being a key player in energy production by converting glucose into pyruvate, which fuels both aerobic and anaerobic pathways (*56*). Notably, glycolysis is important for rapidly dividing cells, including tumor and immune cells, to meet their energy demands. Immune cells predominantly rely on glycolysis when activated, to bolster an inflammatory response, but switch back to oxidative phosphorylation after the inflammation subsides (*57*). This metabolic shift is closely associated with inflammatory signaling, highlighted by increased glycolysis driving inflammatory markers in endothelial cells via HIF1α up-regulation (*58*) and the dampening of NF-κB activation when glycolysis is inhibited (*59*, *60*). Similarly, our findings reveal elevated NF-κB signaling (fig. S7A) and inflammatory marker expression (Fig. 3D and fig. S5) in myoblasts under hypoxic conditions, aligning with known glycolysis-inflammation dynamics. Mechanistically, glycolytic intermediates and enzymes have been implicated in modulating inflammation. For example, the accumulation of phosphoenolpyruvate in T cells encourages a proinflammatory phenotype (*61*, *62*), and lactate boosts proinflammatory activities through NF-κB pathways (*63*, *64*). In addition, certain glycolytic enzymes act as posttranscriptional regulators of inflammatory genes by

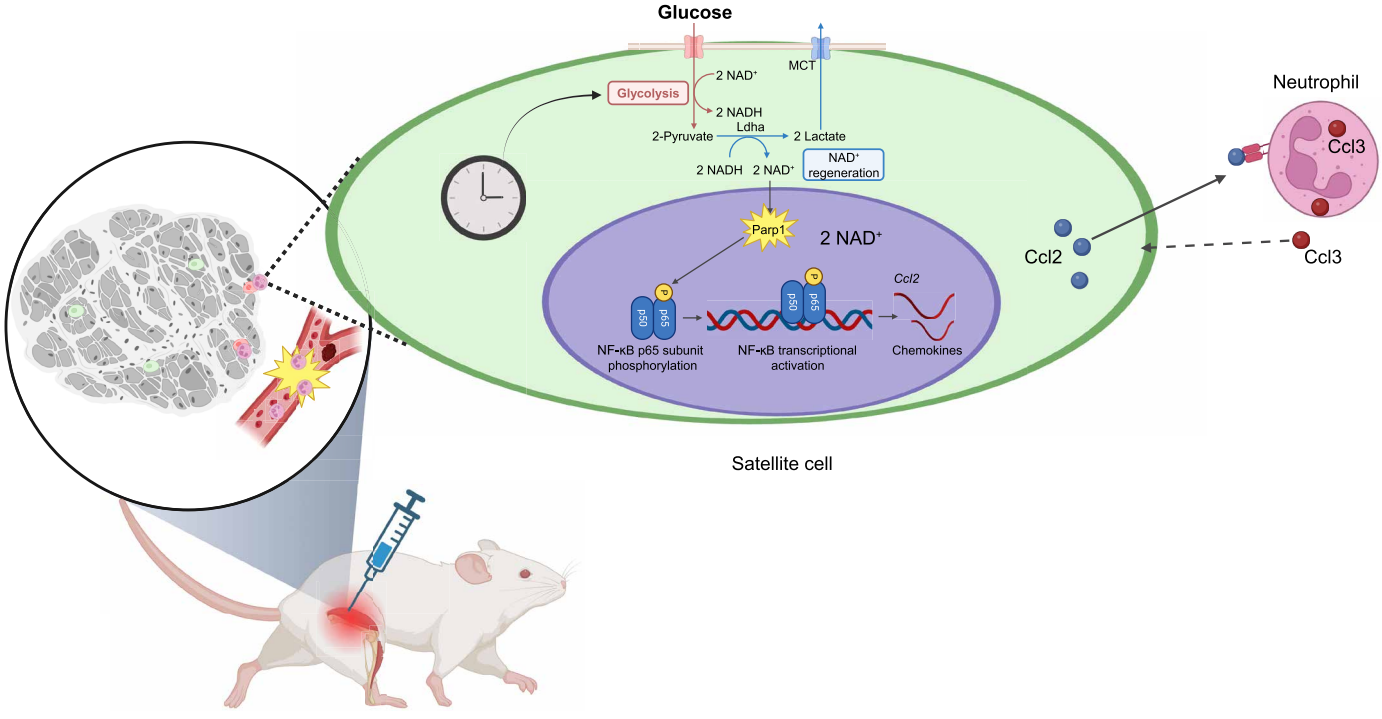

Fig. 7. Proposed model depicting the process underlying TOD-dependent muscle regeneration. Schematic depicting the process underlying TOD-dependent muscle regeneration. Following injury, skeletal muscle experiences passive hypoxia, triggering enhanced anaerobic glycolysis in SCs. The regeneration of cytoplasmic NAD^+ during this process acts as a substrate as activated PARP1, which then activates NF-κB through the phosphorylation of the p65 subunit at serine-536. This activation further promotes the expression of immunomodulator genes (e.g., *Ccl2*), aligning with a peak in neutrophil infiltration into the wounded site. This synchronization facilitates interactions between SCs and neutrophils, reciprocally enhancing SC proliferation and muscle repair efficiency. Given that the glycolysis pathway is regulated by the circadian clock, this signaling cascade contributes to variations in muscle repair efficacy depending on the TOD.

binding to their mRNAs (*65*, *66*). These findings underscore the impact of glycolysis on immune cell activity.

The reason why rapidly proliferating cells discard carbon by expelling pyruvate-converted lactate remains unclear, although recent insights suggest a preference for converting pyruvate to lactate via LDH when the need for NAD^+ regeneration surpasses adenosine triphosphate (ATP) demand (*67*). While glycolysis facilitates NAD^+ regeneration critical for maintaining its flux and ATP production, our study suggests an added role of LDHA-mediated NAD^+ regeneration within SCs to regulate early muscle repair. Like cancer cells, glycolysis dominates in proliferating myoblasts even under highly oxygenated culture conditions (*68*), underscoring its importance in supporting SC proliferation. Nonetheless, given that QSCs take more than 24 hours to commence and complete their first division (*69*), while the rate of glycolysis in SCs is reported to increase as soon as they break quiescence, reaching threefold within 3 hours of activation (*70*), ATP might not be their primary need immediately post-injury. Our findings indicate that beyond supporting glycolysis, NAD^+ regeneration is key for immune modulation, activating PARP and NF-κB pathways to induce chemokine production, thus orchestrating neutrophil recruitment and SC interaction. This mechanism is backed by the exclusive induction of *Parp1* (fig. S7B) and enhanced expression of genes associated with DNA damage responses, a known trigger for PARP1 activation (*71*) (Fig. 1E) in 1dpi ASC versus QSCs. Given the rapid NAD^+-consuming capacity of PARP1 (*72*) and its ability to prioritize NAD^+ over Sirtuin proteins (*73*), our results suggest that alongside sustaining glycolytic flux, NAD^+ regeneration supports PARP1 activation, which may be crucial for immune modulation in the initial muscle regeneration phase. However, this conclusion appears to challenge the established dogma of redox biology. If regenerated NAD^+ is consumed for PARP1 activation, glycolytic flux would be expected to collapse because of insufficient replenishment of NAD(H). We hypothesize that anaerobic NAD^+ regeneration by LDHA plays a critical role in maintaining the NAD^+/NADH redox state, preventing glycolytic collapse under hypoxic conditions. Supporting this, our data demonstrate that galloflavin, a lactate dehydrogenase inhibitor that impedes NAD^+ regeneration, significantly reduced *Ccl2* expression under hypoxia (Fig. 3C). Notably, our RNA sequencing data revealed significant up-regulation of *Nampt* ($\log_2FC = 0.84$, adjusted $P = 9.68 \times 10^{-21}$) in myoblasts after 6 hours of hypoxia. This suggests that, while anaerobic glycolysis is NAD^+ neutral, increased NAD^+ synthesis via the salvage pathway may contribute to maintaining cellular NAD^+ levels during hypoxia. Our data demonstrating temporal increases in intracellular NAD^+ levels in hypoxia-exposed myoblasts support this hypothesis (Fig. 3A). This observation aligns with a previous report showing elevated NAD^+ levels in human umbilical cord endothelial cells under hypoxia, with increases at 10 and 60 min and a significant 57% increase after 120 min of incubation (*74*). Similarly, significant increases in both NAD^+ levels and the NAD^+/NADH ratio were observed in endothelial progenitor cells under hypoxia (*75*). We propose that regenerated NAD^+ contributes at least partially to PARP1 activation, which subsequently activates NF-κB and induces *Ccl2* expression under hypoxic conditions. In addition, newly synthesized NAD^+ via the salvage pathway may further support PARP1 activity and help maintain glycolytic flux, reinforcing this mechanism. Whether lactate plays a role in this process remains an open question that warrants further investigation.

Neutrophils play an indispensable role in the innate immune system, serving as the frontline defense against pathogens (*76*). They navigate from the bone marrow to infection or inflammation sites by adhering to the leukocyte adhesion cascade (*77*). This migration exhibits a circadian rhythm, potentially linked to the cyclic expression of genes related to migration, suggesting that NAD^+ regeneration, triggering chemokine release, contributes to neutrophil recruitment across different muscle cell types. Furthermore, the circadian clock intricately modulates glycolytic activity by controlling the HIF1α-mediated response to hypoxia (*33*, *78*). In particular, our previous research highlighted that *Bmal1* in SCs or myoblasts regulates the expression of critical glycolytic genes, including *Glut1*, *Hk2*, and *Ldha*, influencing glycolysis and the anaerobic regeneration of NAD^+ (*4*). Thus, the circadian regulation of neutrophil infiltration is also influenced by peripheral clock residing in the surrounding cell populations.

Muscle injury leads to the necrosis and degeneration of muscle fibers, accompanied by hematoma formation. Neutrophils rapidly migrate to the injury site within hours of damage (*79*). Studies involving mice, where intraperitoneal injections of antisera targeting neutrophils were used alongside myotoxin injections, highlight the critical role of neutrophils in efficient muscle repair (*80*). Neutrophils could contribute to muscle regeneration by clearing tissue debris (*81*) and by recruiting monocytes and macrophages through the release of inflammatory cytokines and chemokines (*82*). A recent in vitro study further underscored the influence of neutrophils on muscle regeneration. When myoblasts were treated with media conditioned by activated neutrophils, there was a notable promotion of myoblast proliferation and a suppression of differentiation compared to treatment with basal media (*39*). Specifically, the study found that inhibiting the neutrophil-derived factor Ccl3 in the conditioned media nullified the proliferative effects, while blocking Mmp-9 encouraged myoblast differentiation (*39*). Intriguingly, *Ccl3* expression was significantly higher at ZT16 compared to ZT4 in the Neutrophil_1 population on day 1 post-injury ($\log_2FC = 1.636927839$, Adj. *P* value = 0) (fig. S10C), suggesting that the interaction between SCs and neutrophils leads to TOD-dependent variations in SC proliferation. Further studies are needed to understand whether TOD-dependent regulation of neutrophil activity can reciprocally affect SC proliferation and myogenic capacity.

Within the subset of neutrophil chemotaxis–related genes that were up-regulated in ASCs at 1 dpi compared to QSCs, the expression of *Ccl2* showed TOD-dependent variations, being significantly higher in ASCs at ZT16 than at ZT4 (Fig. 4F and fig. S2B). *Ccl2* was the only chemokine gene among the top ligands that exhibited high activity in inducing target gene expression in Neutrophils_1 (Fig. 4E and fig. S10C). CCL2 is recognized as a potent chemoattractant for neutrophils (*21*), and previous study has indicated its capacity to attract substantial neutrophil numbers to the lung even without underlying inflammation (*83*). Moreover, experiments in mice deficient in *Ccl2* have revealed impaired infiltration of monocyte/macrophages, leading to an altered regenerative process that favors adipogenic over myogenic differentiation (*84*, *85*). In addition, a decrease in *Ccl2* expression, resulted from CD8 knockout, has been associated with compromised muscle regeneration and increased fibrosis (*86*). However, these studies did not explore the role of *Ccl2* expressed by SC during muscle regeneration. Our findings, through transplantation of *Ccl2*-overexpressing SC-derived myoblasts, demonstrated an increase in the presence of these exogenous progenitors within the

proliferating muscle stem cell pool of regenerating muscles at day 3 post-injury compared to control myoblasts (Fig. 5I). This highlights the key role of neutrophil interactions in the activation and proliferation of SCs.

The circadian regulation of muscle regeneration has been independently established in prior studies from our group and others (*4*, *5*). While the TOD-dependent differences in muscle repair with cardiotoxin are statistically significant and reproducible, they are not as pronounced as those observed in mice with systemic or SC-conditional core clock gene deletions when assessed histologically at day 7 post-injury (*4*, *5*, *87*). Moreover, one study noted that the initial differences in regenerating fiber size observed between injuries inflicted at ZT14 and ZT2 seem to equalize by day 14 post-injury (*5*). Here, we demonstrate that the effects of TOD of muscle injury can be compounded with repeated injuries. Specifically, repeated injury during the rest period (i.e., ZT4 for a mouse) led to differences in the size of regenerated myofibers, even at 1 month following the last injury event. In addition, this coincided with a trend toward changes in muscle function, reinforcing the long-term negative impact of muscle injury during the rest phase, although further studies are required to establish the exact impact of TOD injury on long-term changes in muscle function. Overall, these findings raise important questions regarding the potential pathological aspects of impaired muscle regeneration in conditions such as obesity, diabetes, and aging, where circadian rhythms are continuously disrupted.

The current study has certain limitations in its experimental design and data interpretation. While our signaling pathway enrichment analysis of QSCs at ZT4 and ZT16 (fig. S9) indicates that circadian regulation in the stem cell transcriptome differs significantly from the transcriptional changes observed in 1-dpi ASCs following injury at ZT4 and ZT16 (Fig. 4C), we acknowledge that we cannot completely exclude the potential influence of circadian phase on gene expression in 1-dpi ASCs. Addressing this limitation would require performing RNA sequencing on ASCs collected at both ZT4 and ZT16 from muscles injured at these respective times. Last, while we observed an increase in total cellular NAD^+ levels in myoblasts following acute hypoxia exposure, the impact of hypoxia and the circadian clock on the free cytonuclear NAD^+ pool—crucial for regulating PARP activity—remains unclear.

In summary, we have revealed a previously unrecognized mechanism that links NAD^+ regeneration during anaerobic glycolysis with neutrophil modulation. This interaction, in turn, affects the activation and proliferation of muscle stem cells, thereby influencing the effectiveness of muscle regeneration. Further research is needed to elucidate the role of clock-regulated NAD^+ metabolism in immune modulation, particularly in the context of acute and chronic disease states.

METHODS

Mice

C57BL/6J mice (#000664) and B6.Cg-Pax7$^{tm1(cre/ERT2)Gaka}$/J mice (#017763) were acquired from The Jackson Laboratory. CytoLbNOX$^{LSL/LSL}$ mice, characterized by a Lox-Stop-Lox (LSL) cassette upstream of CytoLbNOX and an internal ribosomal entry site–linked enhanced GFP, were provided by N. Chandel at Northwestern University. Pax7-zsGreen mice were supplied by M. Kyba at the University of Minnesota. To achieve SC-conditional expression of CytoLbNOX, we crossed CytoLbNOX$^{LSL/LSL}$ mice with B6.Cg-Pax7$^{tm1(cre/ERT2)Gaka}$/J mice, resulting in CytoLbNOX$^{LSL/LSL}$Pax7$^{tm1(cre/ERT2)}$ and control CytoLbNOX$^{+/+}$Pax7$^{tm1(cre/ERT2)}$ mice. CytoLbNOX expression was initiated through five consecutive daily intraperitoneal injections of tamoxifen (20 mg/ml in corn oil, 100 mg/kg body weight). The mice were housed under a 12:12 light:dark cycle. All procedures were carried out with male mice aged 8 to 12 weeks, in strict accordance with the guidelines of the Institutional Animal Care and Use Committee at Northwestern University (protocol #IS00026931).

Neutrophil depletion

Neutrophil depletion in vivo was conducted through intraperitoneal injections of 300 μg the 1A8 monoclonal anti-mouse Ly6G antibody, administered daily over a period of three consecutive days. As a control, the corresponding rat IgG2a isotype control antibody was injected in a similar manner. The efficacy of neutrophils and monocyte depletion post-antibody treatment was verified by flow cytometry analysis.

Skeletal muscle injury

Cardiotoxin-induced TA muscle injury was conducted according to methodologies previously described (*4*). Mice underwent anesthesia via intraperitoneal administration of a ketamine (80 mg/kg) and xylazine (10 mg/kg) mixture. Subsequent to the removal of fur from the injection site, TA muscles received a 50-μl injection of a 10 μM cardiotoxin solution in saline, delivered using a 0.5-ml BD insulin syringe.

Histology

To evaluate muscle regeneration, TA muscles were harvested at indicated time points after injury and enveloped in a thin layer of Tissue-Tek O.C.T. compound. The samples were snap-frozen in liquid nitrogen–chilled isopentane and preserved at −80°C for later processing. Continuous 10-μm-thick cross sections of the frozen TAs were prepared using a Leica CM1860 cryostat. For hematoxylin and eosin staining, sections were air-dried overnight at room temperature. Subsequent rehydration in phosphate-buffered saline (PBS) for 5 min was followed by fixation in 10% formalin. The nuclei were then stained with hematoxylin for 5 min, with excess stain removed by rinsing under tap water for 5 min and briefly dipping in clarifier. Eosin was applied for 30 s to stain the cytoplasm and connective tissues. The sections were dehydrated through a graded series of ethanol, cleared in xylene, and mounted with Permount mounting medium. The prepared slides were examined using a Keyence BZ-X800 microscope. Cross-sectional area of myofibers was quantified using FIJI software (*88*) with LabelsToROIs plugin (*89*).

Immunohistochemistry

Tissue sections were allowed to air-dry for 30 min at room temperature and were then fixed with 4% paraformaldehyde and permeabilized using 0.25% Triton X-100 for 15 min. For blocking, sections were treated with PBS containing 5% goat serum, 2% bovine serum albumin (BSA), and 1% Tween-20 for 1 hour. This was followed by an overnight incubation at 4°C with primary antibodies, including anti-laminin (1:100), anti–Ly-6G (1:100) in a diluent buffer of PBS with 0.5% goat serum, 2% BSA, and 1% Tween-20. After washing in PBS thrice, the sections were incubated with an Alexa Fluor–conjugated secondary antibodies at a 1:1000 dilution for 1 hour at room temperature. Sections were then mounted using VectaShield HardSet antifade mounting medium with 4′,6-diamidino-2-phenylindole (DAPI) for visualization under a Keyence BZ-X800 microscope.

Immunofluorescence

Primary myoblasts were rinsed with ice-cold PBS and fixed with methanal for 15 min at −20°C. They were then permeabilized using 0.2% Triton X-100 and blocked to prevent nonspecific binding with 1% BSA for 1 hour at room temperature. This was followed by incubation with an anti-Poly(ADP-ribose) polyclonal antibody at a 1:500 dilution overnight at 4°C. The following day, the myoblasts were washed thrice with PBS and incubated with an Alexa Fluor 594–conjugated goat anti-rabbit IgG secondary antibody at a 1:1000 dilution in 1% BSA for 1 hour at room temperature. Nuclear staining was performed with DAPI (5 μg/ml in PBS) ffor 5 min, and the samples were visualized under an Evos FL cell-imaging microscope.

In vivo muscle contractility measurement

Mice were anesthetized using a precision vaporizer (Somnoflo; Kent Scientific) with initial induction of 2.5% isoflurane. After induction, a mouse was transferred to a 37°C motor stage (Aurora Scientific), and the appropriate leg was shaved from ankle to hip.

Dorsiflexion torque was measured as previously described (*90*), with the foot fixed to the footplate attached to a 300C series dual mode lever. Briefly, two needle electrodes were placed subcutaneously on either side of the peroneal nerve to activate dorsiflexors. Then, a torque-frequency curve was generated from 10 to 150 Hz as previously described (*90*). Torque was recorded at each frequency. ZT4 mice (injured and uninjured) were tested at 9:00 a.m., while ZT16 mice (injured/uninjured) were tested at 1 p.m.

Retrovirus production

The cDNA open reading frame for mouse chemokine (C-C motif) ligand 2 (Ccl2) was ordered from GenScript and subsequently amplified by PCR using Phusion High-Fidelity DNA Polymerase & dNTP Mix. The amplified sequence was cloned between the Xho I and EcoR I restriction sites of the retroviral mammalian expression vector MIGR1 (*91*). To produce retrovirus carrying the Ccl2 gene, 293T cells were transfected with a DNA comprising 1.5 μg of pCL-Eco (*92*) and 2.5 μg MIGR1-Ccl2, or MIGR1 vector using Lipofectamine 3000 Transfection Reagent according to the provided instructions. The retrovirus-enriched supernatant was collected 24 hours post-transfection and was then filtered through a syringe filter with a pore size of 0.45 μm to ensure purity.

Muscle cell isolation

For the in vitro culture of myoblasts, muscle cells were extracted from the entire hindlimb muscles. Bulk RNA sequencing involved the use of Pax7-zsgreen mice, which were sequentially perfused with 50 ml of ice-cold PBS, followed by 50 ml of mild fixative (0.5% paraformaldehyde), and subsequently quenched with 50 ml of 2 M glycine, as previously reported (*43*, *93*). SCs were collected from the TA muscles on both sides. For single-cell RNA sequencing, mononucleated muscle cells were isolated from TA muscles on both hindlimbs. Muscle cell preparation was performed by following previously established procedures (*4*). Specifically, excised muscle tissues were digested in Hams F-10 medium supplemented with collagenase D (5 mg/ml) and dispase II (5 mg/ml) for 30 min at 37°C with shaking at 500 rpm. The enzymatic digestion was terminated by adding a fivefold volume of ice-cold cell suspension buffer [Ham's F-10 with 10% fetal bovine serum (FBS) and 3 mM EDTA]. The digested muscle tissue was then subjected to mechanical dissociation through vigorous pipetting (20 times with a 10-ml pipette) to release MuSCs from the myofibers. The cell suspension was filtered through 70- and 40-μm nylon mesh strainers in sequence, and the filtrate was collected in a 15-ml conical tube and centrifuged at 500*g* for 5 min. The resulting cell pellets were resuspended in 1 ml of Pre-Sort buffer, with propidium iodide serving as an indicator of cell viability. For bulk RNA sequencing, zsgreen-positive mononuclear SCs were sorted using a BD FACSAria II cell sorter.

Myoblasts preparation was performed with slight modification to a previously established preplating technique (*94*). Initially, the crude suspension was seeded and expanded on a 60-mm dish coated with Matrigel, in myoblast growth medium consisting of Hams F-10 with 20% FBS, 1% penicillin-streptomycin (PS), and basic fibroblast growth factor (bFGF, 2.5 ng/ml) for 3 days. Following this, the cells underwent trypsinization and were subjected to a preplating process on a regular tissue culture–treated 60-mm dish for 1 hour, before being transferred to another Matrigel-coated dish. This procedure was repeated three times to reduce the presence of non-myoblast cells. The resultant myoblast-enriched cultures were then maintained in a growth medium composed of Dulbecco's modified Eagle's medium (DMEM)/Hams F-10 (1:1) with 20% FBS, 1% PS, and bFGF (2.5 ng/ml). The purity of myoblast, verified to be over 95% using immunofluorescence with a Pax7-antibody (Developmental Studies Hybridoma Bank), underscored the effectiveness of this method. Induction of Cyto-LbNOX was conducted no sooner than 48 hours after primary myoblasts were infected with either an adenovirus expressing Cre recombinase (Adv-Cre) or a control empty vector (Adv-Ctrl) from Vector Biolabs.

SC transplantation

SCs from wild-type C57BL/6 mice were isolated on the basis of a combination of cell surface markers $CD45^{-}CD31^{-}Sca1^{-}VcamI^{+}$ (*50*). These cells were then transduced overnight with either a control or *Ccl2*-expressing retrovirus, in the presence of polybrene (8 μg/ml) within wells coated with Matrigel. To prepare for transplantation, TA muscles in recipient wild-type C57BL/6 mice underwent injury preconditioning with a 50 solution of 10 μM cardiotoxin solution in saline, administered 6 hours before cell transplantation. Subsequently, 10,000 SCs, transduced with either control or *Ccl2*-expressing retrovirus as denoted by GFP expression, were sorted, and intramuscularly injected into the pre-injured TA muscles on each side. The cells were delivered in a small volume of 15 μl using 0.3-ml insulin syringes to ensure precise administration.

Bulk RNA sequencing

Total RNA was extracted from in vivo light-fixed Pax7-$zsgreen^{+}$ SCs using the miRNeasy FFPE Kit, adhering to the supplied instructions with a crucial modification that the digestion of RNA by proteinase K was performed at 56°C for 1 hour as previously reported (*43*). For the initial double-stranded cDNA synthesis, amounts ranging from 10 pg to 10 ng of total RNA were used using the SMART-seq v4 Ultra Low Input RNA Kit from Takara Bio, following the protocol included within the kit. After PCR amplification, the resulting cDNA was purified using the AMPure XP beads. This purified cDNA underwent assessment using the Agilent 2100 Bioanalyzer paired with Agilent's High-Sensitivity DNA Kit. Three hundred picograms of the full-length cDNA, derived from the SMART-seq v4 Ultra Low-Input RNA Kit, was then prepared for sequencing using the Nextera XT DNA Library Preparation Kit. The PCR-amplified, size-selected cDNA fragments were both visualized and quantified using the

Agilent 2100 Bioanalyzer in conjunction with Agilent's High-Sensitivity DNA Kit, and the Qubit dsDNA HS Assay Kit, respectively. The pooled libraries were sequenced using NovaSeq 6000 SP Reagent Kit v1.5 (100 cycles) on a NovaSeq 6000 system, executing a paired-end run [51 base pairs (bp), repeated twice] to achieve a sequencing depth of approximately 50 million reads per sample.

RNA sequencing analysis

Raw BCL files were processed into demultiplexed, paired-end FastQ files using bcl2fastq conversion software (v2.19.1). Subsequently, adaptor sequences were trimmed from these files using Trimmomatic (v0.33) (*95*). The processed reads were then aligned to the mm10 *Mus musculus* reference genome using the STAR aligner (v2.5.2) (*96*). Gene alignment counts were determined using RSEM (v1.3.3) (*97*). Isoform-level quantifications obtained from RSEM were integrated into DESeq2 (*98*) for differential expression analysis, facilitated by the tximport package (*99*), with settings adjusted to "rsem" and both "txIn" and "txOut" flags set to "TRUE." The DESeq2's results function was used to identify differentially expressed genes, which were then subjected to multiple testing correction using the Benjamini-Hochberg method to calculate adjusted *P* values. Visualization of gene counts for DEGs was achieved using the pheatmap (v1.0.12) and EnhancedVolcano (version 1.2.0) packages within R (v3.6.1). Last, KEGG and Elsevier Pathway Collection pathways enrichment as well as gene ontology analyses were conducted using EnrichR (*100*), ShinyGO (v0.66) (*101*), and Fast Gene Set Enrichment Analysis (doi: https://doi.org/10.1101/060012).

Single-cell RNA sequencing

Muscle cells were isolated from both intact and cardiotoxin-injured TA muscles on both sides of the hindlimb at ZT4 and ZT16 on days 0 (intact), 1, and 3 post-injuries. The initial step involved the elimination of red blood cells using RBC Lysis Buffer, followed by resuspension of the muscle cells in 1 ml of Pre-Sort buffer. Cell viability was assessed with propidium iodide. To ensure accurate cell sorting, doublet exclusion was strictly conducted by comparing the height to the area for both forward scatter and side scatter signals. Approximately 100,000 propidium iodide–negative single muscle cells were then sorted from each sample using a BD FACSAria II cell sorter. Subsequent sample processing was completed at the NUSeq Core Facility at Northwestern University. Briefly, the cell number and viability were further evaluated using the Nexcelom Cellometer Auto2000 using the acrodine orange/propidium iodide (AO/PI) fluorescent staining method. For single-cell RNA sequencing, 10,000 cells from each condition were loaded into a Chromium Controller (10X Genomics) using a Chromium Next GEM Chip G (10X Genomics). These were processed to form single-cell gel beads in the emulsion (GEM) following the manufacturer's instructions. cDNA synthesis and library preparation were performed using the Chromium Next GEM Single Cell 3′ Reagent Kits v3.1 and Single Index Kit T Set A (10X Genomics) according to the provided manual. Quality control for constructed library was performed by Agilent Bioanalyzer High Sensitivity DNA kit (Agilent Technologies) and Qubit DNA HS assay kit for qualitative and quantitative analysis, respectively. The multiplexed libraries were pooled and sequenced using NovaSeq 6000 S1 Reagent Kit v1.5 (100 cycles) on Illumina NovaSeq 6000 sequencer with 2 × 50 paired-end kits using the following read length: 28 bp Read1 for cell barcode and unique molecular identifier, 8 bp I7 index for sample index, and 91 bp Read2 for transcript.

Single-cell RNA sequencing analysis

For demultiplexing and read counting, Cell Ranger (v1.0.0) was used. The Seurat package (v4.0.0) (*102*) in R facilitated data preprocessing and visualization. Quality control measures and cell selection criteria were stringently applied; cells exhibiting less than 200 or more than 6000 feature counts (for cells from intact and 1 dpi injured TA muscles) or exceeding 7500 feature counts (for cells from 3 dpi injured TA muscles) were excluded. Genes detected in fewer than three cells were discarded. To account for low-quality and dying cells typically showing high mitochondrial content, cells were selected on the basis of a threshold where only those with less than 5% of reads mapping to the mitochondrial were retained. In addition, MALAT1, a highly expressed large noncoding nuclear gene, was excluded from downstream analyses.

To identify potential doublets, a two-tiered approach was adopted as per Germain *et al.* (*103*): Initially, scDblFinder (v1.4.0) predicted doublets using default settings, followed by manual identification based on the expression of marker genes from different cell types. After refining the dataset to remove low-quality cells, normalization of single cells from all six samples was carried out using NormalizeData function, and samples were integrated using a canonical correlation analysis based anchor method. The dataset was further adjusted by regressing out the difference between G2-M and S phase scores, effectively preserving distinctions between noncycling and cycling cells while ignoring variations among proliferating cells. Clustering was performed using the first 50 principal components, derived from the top 2000 most variable features, in a K-nearest neighbor graph with a resolution at 0.5. Subsequently, UMAP provided nonlinear dimensional reduction and visualization of clusters. Differentially expressed features across clusters were identified using FindAllMarkers function. Cell identities within each cluster were ascribed on the basis of canonical marker genes for skeletal muscle cells, as described in previous studies (*14*, *15*), and markers from the CellMarker 2.0 database (*13*). Differential gene expression analyses between clusters used the FindMarkers function, setting a threshold of 0.25 for log fold change and 0.05 for the adjusted *P* value. Cell lineage and pseudotime inference analysis within MuSC subclusters were conducted using the Slingshot package (*46*), with downstream gene expression along trajectories analyzed via the tradeSeq package (*47*). Intercellular interaction analysis and visualization among the two neutrophil and MuSC populations at various days post-injury were performed using the CellChat package (*20*) with standard parameters. To examine TOD-dependent variations in communication between MuSC and neutrophils, the NicheNet package (*34*) was used, positioning MuSC as the "signal sender" to explore the ligands affecting neutrophils.

Western blotting

Myoblast whole-cell lysates were prepared using CelLytic mammalian tissue lysis reagent, with the addition of protease inhibitors, to ensure protein integrity. For the preparing total protein lysates from muscle tissue, each snap-frozen TA muscle specimen was placed in 500 µl of CelLytic mammalian tissue lysis reagent supplemented with protease inhibitors and homogenized using a TissueLyser II apparatus from Qiagen to achieve uniform cell disruption. Subsequent to homogenization, protein concentrations were determined using the DC Protein Assay Kit, enabling accurate loading for SDS–polyacrylamide gel electrophoresis. Proteins separated by electrophoresis were then transferred onto 0.45-µm nitrocellulose membranes for immunoblotting. For the detection of specific proteins, the membranes were

incubated overnight at 4°C with primary antibodies, including anti-HIF1α (1:1000 dilution), phospho–NF-κB p65 (Ser^{536}; 1:1000 dilution), NF-κB p65 (1:1000 dilution), PAR/pADPr (1:1000 dilution), and β-actin (1:10,000 dilution). Following primary antibody incubation, the membranes were washed and then incubated with appropriate horseradish peroxidase–conjugated secondary antibodies. The protein bands were visualized using an enhanced chemiluminescence detection system, allowing for the quantitative analysis of protein expression levels.

RNA extraction and real-time qPCR

For the qPCR analysis, total RNA was isolated from myoblasts using TRIzol Reagent, adhering strictly to the guidelines provided by the manufacturer. The quality and quantity of the extracted total RNA were assessed using the NanoDrop 2000 Spectrophotometers. RNA samples displaying an OD260/280 ratio greater than 1.80 were deemed suitable and thus advanced to the first strand cDNA synthesis using Applied Biosystems High-Capacity cDNA Reverse Transcription Kit, following the instructions detailed in the kit's protocol. The subsequent real-time qPCR was performed using iTaq Universal SYBR Green Supermix from Bio-Rad on a CFX Opus 384 Real-Time PCR System.

ELISA

The concentration of CCL2 released by myoblasts into the culture medium was quantified using the mouse MCP-1 ProQuantum Immunoassay Kit following the instructions provided by the manufacturer.

Utilization of artificial intelligence tools

Artificial intelligence (AI) tools were used within this manuscript as follows. ChatGPT-4o was used to check grammar and clarity of portions of the manuscript. The prompt given was: "Edit passage of manuscript for grammar and clarity."

Supplementary Materials

This PDF file includes:

Figs. S1 to S12
Table S1

REFERENCES AND NOTES

1. J. S. Takahashi, Transcriptional architecture of the mammalian circadian clock. *Nat. Rev. Genet.* **18**, 164–179 (2017).
2. J. Bass, M. A. Lazar, Circadian time signatures of fitness and disease. *Science* **354**, 994–999 (2016).
3. J. Bass, J. S. Takahashi, Circadian integration of metabolism and energetics. *Science* **330**, 1349–1354 (2010).
4. P. Zhu, N. X. Hamlish, A. V. Thakkar, A. W. T. Steffeck, E. J. Rendleman, N. H. Khan, N. J. Waldeck, A. W. DeVilbiss, M. S. Martin-Sandoval, T. P. Mathews, N. S. Chandel, C. B. Peek, BMAL1 drives muscle repair through control of hypoxic NAD^+ regeneration in satellite cells. *Genes Dev.* **36**, 149–166 (2022).
5. N. Katoku-Kikyo, E. Paatela, D. L. Houtz, B. Lee, D. Munson, X. Wang, M. Hussein, J. Bhatia, S. Lim, C. Yuan, Y. Asakura, A. Asakura, N. Kikyo, Per1/Per2–Igf2 axis–mediated circadian regulation of myogenic differentiation. *J. Cell Biol.* **220**, e202101057 (2021).
6. S. B. P. Chargé, M. A. Rudnicki, Cellular and molecular regulation of muscle regeneration. *Physiol. Rev.* **84**, 209–238 (2004).
7. H. Yin, F. Price, M. A. Rudnicki, Satellite cells and the muscle stem cell niche. *Physiol. Rev.* **93**, 23–67 (2013).
8. J. Torres-Ruiz, B. Alcalá-Carmona, R. Alejandre-Aguilar, D. Gómez-Martín, Inflammatory myopathies and beyond: The dual role of neutrophils in muscle damage and regeneration. *Front. Immunol.* **14**, 1113214 (2023).
9. C. Latroche, M. Weiss-Gayet, L. Muller, C. Gitiaux, P. Leblanc, S. Liot, S. Ben-Larbi, R. Abou-Khalil, N. Verger, P. Bardot, M. Magnan, F. Chrétien, R. Mounier, S. Germain, B. Chazaud, Coupling between myogenesis and angiogenesis during skeletal muscle regeneration is stimulated by restorative macrophages. *Stem Cell Reports* **9**, 2018–2033 (2017).
10. C. Tecchio, M. A. Cassatella, Neutrophil-derived chemokines on the road to immunity. *Semin. Immunol.* **28**, 119–128 (2016).
11. J. A. Read, V. J. Winter, C. M. Eszes, R. B. Sessions, R. L. Brady, Structural basis for altered activity of M- and H-isozyme forms of human lactate dehydrogenase. *Proteins* **43**, 175–185 (2001).
12. L. Forcina, M. Cosentino, A. Musarò, Mechanisms regulating muscle regeneration: Insights into the interrelated and time-dependent phases of tissue healing. *Cells* **9**, 1297 (2020).
13. C. Hu, T. Li, Y. Xu, X. Zhang, F. Li, J. Bai, J. Chen, W. Jiang, K. Yang, Q. Ou, X. Li, P. Wang, Y. Zhang, CellMarker 2.0: An updated database of manually curated cell markers in human/mouse and web tools based on scRNA-seq data. *Nucleic Acids Res.* **51**, D870–D876 (2023).
14. S. N. Oprescu, F. Yue, J. Qiu, L. F. Brito, S. Kuang, Temporal dynamics and heterogeneity of cell populations during skeletal muscle regeneration. *iScience* **23**, 100993 (2020).
15. A. J. De Micheli, E. J. Laurilliard, C. L. Heinke, H. Ravichandran, P. Fraczek, S. Soueid-Baumgarten, I. D. Vlaminck, O. Elemento, B. D. Cosgrove, Single-cell analysis of the muscle stem cell hierarchy identifies heterotypic communication signals involved in skeletal muscle regeneration. *Cell Rep.* **30**, 3583–3595.e5 (2020).
16. P. Delobel, B. Ginter, E. Rubio, K. Balabanian, G. Lazennec, CXCR2 intrinsically drives the maturation and function of neutrophils in mice. *Front. Immunol.* **13**, 1005551 (2022).
17. A. M. Cieutat, P. Lobel, J. T. August, L. Kjeldsen, H. Sengeløv, N. Borregaard, D. F. Bainton, Azurophilic granules of human neutrophilic leukocytes are deficient in lysosome-associated membrane proteins but retain the mannose 6-phosphate recognition marker. *Blood* **91**, 1044–1058 (1998).
18. K. Pittman, P. Kubes, Damage-associated molecular patterns control neutrophil recruitment. *J. Innate Immun.* **5**, 315–323 (2013).
19. J. Wang, Neutrophils in tissue injury and repair. *Cell Tissue Res.* **371**, 531–539 (2018).
20. S. Jin, C. F. Guerrero-Juarez, L. Zhang, I. Chang, R. Ramos, C.-H. Kuan, P. Myung, M. V. Plikus, Q. Nie, Inference and analysis of cell-cell communication using CellChat. *Nat. Commun.* **12**, 1088 (2021).
21. J. W. Griffith, C. L. Sokol, A. D. Luster, Chemokines and chemokine receptors: Positioning cells for host defense and immunity. *Immunology* **32**, 659–702 (2014).
22. Z. Chen, F. Han, Y. Du, H. Shi, W. Zhou, Hypoxic microenvironment in cancer: Molecular mechanisms and therapeutic interventions. *Signal Transduct. Target. Ther.* **8**, 70 (2023).
23. J. Korbecki, K. Kojder, K. Barczak, D. Simińska, I. Gutowska, D. Chlubek, I. Baranowska-Bosiacka, Hypoxia alters the expression of CC chemokines and cc chemokine receptors in a tumor–A literature review. *Int. J. Mol. Sci.* **21**, 5647 (2020).
24. D. V. Titov, V. Cracan, R. P. Goodman, J. Peng, Z. Grabarek, V. K. Mootha, Complementation of mitochondrial electron transport chain by manipulation of the NAD^+/NADH ratio. *Science* **352**, 231–235 (2016).
25. M. Manerba, M. Vettraino, L. Fiume, G. Di Stefano, A. Sartini, E. Giacomini, R. Buonfiglio, M. Roberti, M. Recanatini, Galloflavin (CAS 568-80-9): A novel inhibitor of lactate dehydrogenase. *ChemMedChem* **7**, 311–317 (2012).
26. J. Landry, A. Sutton, S. T. Tafrov, R. C. Heller, J. Stebbins, L. Pillus, R. Sternglanz, The silencing protein SIR2 and its homologs are NAD-dependent protein deacetylases. *Proc. Natl. Acad. Sci. U.S.A.* **97**, 5807–5811 (2000).
27. S. Imai, C. M. Armstrong, M. Kaeberlein, L. Guarente, Transcriptional silencing and longevity protein Sir2 is an NAD-dependent histone deacetylase. *Nature* **403**, 795–800 (2000).
28. R. A. Frye, Characterization of five human cDNAs with homology to the yeast SIR2 gene: Sir2-like proteins (Sirtuins) metabolize NAD and may have protein ADP-ribosyltransferase activity. *Biochem. Biophys. Res. Commun.* **260**, 273–279 (1999).
29. F. J. Oliver, J. M. Murcia, C. Nacci, P. Decker, R. Andriantsitohaina, S. Muller, G. de la Rubia, J. C. Stoclet, G. de Murcia, Resistance to endotoxic shock as a consequence of defective NF-κB activation in poly (ADP-ribose) polymerase-1 deficient mice. *EMBO J.* **18**, 4446–4454 (1999).
30. I. Racz, K. Tory, F. Gallyas, Z. Berente, E. Osz, L. Jaszlits, S. Bernath, B. Sumegi, G. Rabloczky, P. Literati-Nagy, BGP-15—a novel poly(ADP-ribose) polymerase inhibitor—Protects against nephrotoxicity of cisplatin without compromising its antitumor activity. *Biochem. Pharmacol.* **63**, 1099–1111 (2002).
31. P. G. Jagtap, G. J. Southan, E. Baloglu, S. Ram, J. G. Mabley, A. Marton, A. Salzman, C. Szabó, The discovery and synthesis of novel adenosine substituted 2,3-dihydro-1H-isoindol-1-ones: Potent inhibitors of poly(ADP-ribose) polymerase-1 (PARP-1). *Bioorg. Med. Chem. Lett.* **14**, 81–85 (2004).
32. G. Solanas, F. O. Peixoto, E. Perdiguero, M. Jardí, V. Ruiz-Bonilla, D. Datta, A. Symeonidi, A. Castellanos, P.-S. Welz, J. M. Caballero, P. Sassone-Corsi, P. Muñoz-Cánoves, S. A. Benitah, Aged stem cells reprogram their daily rhythmic functions to adapt to stress. *Cell* **170**, 678–692.e20 (2017).

33. C. B. Peek, D. C. Levine, J. Cedernaes, A. Taguchi, Y. Kobayashi, S. J. Tsai, N. A. Bonar, M. R. McNulty, K. M. Ramsey, J. Bass, circadian clock interaction with HIF1α mediates oxygenic metabolism and anaerobic glycolysis in skeletal muscle. *Cell Metab.* **25**, 86–92 (2017).
34. R. Browaeys, W. Saelens, Y. Saeys, NicheNet: Modeling intercellular communication by linking ligands to target genes. *Nat. Methods* **17**, 159–162 (2020).
35. C. Beaulé, D. Granados-Fuentes, L. Marpegan, E. D. Herzog, In vitro circadian rhythms: Imaging and electrophysiology. *Essays Biochem.* **49**, 103–117 (2011).
36. M. Izumo, C. H. Johnson, S. Yamazaki, Circadian gene expression in mammalian fibroblasts revealed by real-time luminescence reporting: Temperature compensation and damping. *Proc. Natl. Acad. Sci. U.S.A.* **100**, 16089–16094 (2003).
37. K. Yagita, K. Horie, S. Koinuma, W. Nakamura, I. Yamanaka, A. Urasaki, Y. Shigeyoshi, K. Kawakami, S. Shimada, J. Takeda, Y. Uchiyama, Development of the circadian oscillator during differentiation of mouse embryonic stem cells in vitro. *Proc. Natl. Acad. Sci. U.S.A.* **107**, 3846–3851 (2010).
38. C. B. Peek, K. M. Ramsey, D. C. Levine, B. Marcheva, M. Perelis, J. Bass, Circadian regulation of cellular physiology. *Methods Enzym.* **552**, 165–184 (2015).
39. B. R. Seo, C. J. Payne, S. L. McNamara, B. R. Freedman, B. J. Kwee, S. Nam, I. de Lázaro, M. Darnell, J. T. Alvarez, M. O. Dellacherie, H. H. Vandenburgh, C. J. Walsh, D. J. Mooney, Skeletal muscle regeneration with robotic actuation–mediated clearance of neutrophils. *Sci. Transl. Med.* **13**, eabe8868 (2021).
40. K. Takubo, G. Nagamatsu, C. I. Kobayashi, A. Nakamura-Ishizu, H. Kobayashi, E. Ikeda, N. Goda, Y. Rahimi, R. S. Johnson, T. Soga, A. Hirao, M. Suematsu, T. Suda, Regulation of glycolysis by Pdk functions as a metabolic checkpoint for cell cycle quiescence in hematopoietic stem cells. *Cell Stem Cell* **12**, 49–61 (2013).
41. C. T. J. van Velthoven, A. de Morree, I. M. Egner, J. O. Brett, T. A. Rando, Transcriptional profiling of quiescent muscle stem cells in vivo. *Cell Rep.* **21**, 1994–2004 (2017).
42. L. Machado, J. E. de Lima, O. Fabre, C. Proux, R. Legendre, A. Szegedi, H. Varet, L. R. Ingerslev, R. Barrès, F. Relaix, P. Mourikis, In situ fixation redefines quiescence and early activation of skeletal muscle stem cells. *Cell Rep.* **21**, 1982–1993 (2017).
43. L. Yue, R. Wan, S. Luan, W. Zeng, T. H. Cheung, Dek modulates global intron retention during muscle stem cells quiescence exit. *Dev. Cell* **53**, 661–676.e6 (2020).
44. H. AlSudais, N. Wiper-Bergeron, Contaminating reactivity of a monoclonal CCAAT/enhancer binding protein β antibody in differentiating myoblasts. *BMC. Res. Notes* **12**, 717 (2019).
45. A. E. Okafor, X. Lin, C. Situ, X. Wei, Y. Xiang, X. Wei, Z. Wu, Y. Diao, Single-cell chromatin accessibility profiling reveals a self-renewing muscle satellite cell state. *J. Cell Biol.* **222**, e202211073 (2023).
46. K. Street, D. Risso, R. B. Fletcher, D. Das, J. Ngai, N. Yosef, E. Purdom, S. Dudoit, Slingshot: Cell lineage and pseudotime inference for single-cell transcriptomics. *BMC Genomics* **19**, 477 (2018).
47. K. V. den Berge, H. R. de Bézieux, K. Street, W. Saelens, R. Cannoodt, Y. Saeys, S. Dudoit, L. Clement, Trajectory-based differential expression analysis for single-cell sequencing data. *Nat. Commun.* **11**, 1201 (2020).
48. L. Xie, A. Yin, A. S. Nichenko, A. M. Beedle, J. A. Call, H. Yin, Transient HIF2A inhibition promotes satellite cell proliferation and muscle regeneration. *J. Clin. Invest.* **128**, 2339–2355 (2018).
49. D. Bosnakovski, Z. Xu, W. Li, S. Thet, O. Cleaver, R. C. R. Perlingeiro, M. Kyba, Prospective isolation of skeletal muscle stem cells with a Pax7 reporter. *Stem Cells* **26**, 3194–3204 (2008).
50. L. Liu, T. H. Cheung, G. W. Charville, T. A. Rando, Isolation of skeletal muscle stem cells by fluorescence-activated cell sorting. *Nat. Protoc.* **10**, 1612–1624 (2015).
51. Z. A. Malik, K. A. B. Davies, E. C. R. Hall, J. Barrett, S. A. Pullinger, R. M. Erskine, S. O. Shepherd, Z. Iqbal, B. J. Edwards, J. G. Burniston, Diurnal differences in human muscle isometric force in vivo are associated with differential phosphorylation of sarcomeric M-band proteins. *Proteomes* **8**, 22 (2020).
52. M. Sedliak, T. Finni, S. Cheng, T. Haikarainen, K. Häkkinen, Diurnal variation in maximal and submaximal strength, power and neural activation of leg extensors in men: Multiple sampling across two consecutive days. *Int. J. Sports Med.* **29**, 217–224 (2008).
53. R. E. Kahn, R. L. Lieber, G. Meza, F. Dinnunhan, O. Lacham-Kaplan, S. Dayanidhi, J. A. Hawley, Time-of-day effects on ex vivo muscle contractility following short-term satellite cell ablation. *Am. J. Physiol.-Cell Physiol.* **327**, C213–C219 (2024).
54. D. Kemler, C. A. Wolff, K. A. Esser, Time-of-day dependent effects of contractile activity on the phase of the skeletal muscle clock. *J. Physiol.* **598**, 3631–3644 (2020).
55. C. M. Douglas, S. J. Hesketh, K. A. Esser, Time of day and muscle strength: A circadian output? *Phys. Ther.* **36**, 44–51 (2021).
56. N. S. Chandel, Glycolysis. *Cold Spring Harb. Perspect. Biol.* **13**, a040535 (2021).
57. G. Soto-Heredero, M. M. Gómez de las Heras, E. Gabandé-Rodríguez, J. Oller, M. Mittelbrunn, Glycolysis – A key player in the inflammatory response. *FEBS J.* **287**, 3350–3369 (2020).
58. D. Wu, R.-T. Huang, R. B. Hamanaka, M. Krause, M.-J. Oh, C.-H. Kuo, R. Nigdelioglu, A. Y. Meliton, L. Witt, G. Dai, M. Civelek, N. R. Prabhakar, Y. Fang, G. M. Mutlu, *HIF-1*α is required for disturbed flow-induced metabolic reprogramming in human and porcine vascular endothelium. *eLife* **6**, e25217 (2017).
59. R. Zhang, R. Li, Y. Liu, L. Li, Y. Tang, The glycolytic enzyme PFKFB3 controls TNF-α-induced endothelial proinflammatory responses. *Inflammation* **42**, 146–155 (2019).
60. A. R. Cantelmo, L.-C. Conradi, A. Brajic, J. Goveia, J. Kalucka, A. Pircher, P. Chaturvedi, J. Hol, B. Thienpont, L.-A. Teuwen, S. Schoors, B. Boeckx, J. Vriens, A. Kuchnio, K. Veys, B. Cruys, L. Finotto, L. Treps, T. E. Stav-Noraas, F. Bifari, P. Stapor, I. Decimo, K. Kampen, K. D. Bock, G. Haraldsen, L. Schoonjans, T. Rabelink, G. Eelen, B. Ghesquière, J. Rehman, D. Lambrechts, A. B. Malik, M. Dewerchin, P. Carmeliet, Inhibition of the glycolytic activator PFKFB3 in endothelium induces tumor vessel normalization, impairs metastasis, and improves chemotherapy. *Cancer Cell* **30**, 968–985 (2016).
61. P.-C. Ho, J. D. Bihuniak, A. N. Macintyre, M. Staron, X. Liu, R. Amezquita, Y.-C. Tsui, G. Cui, G. Micevic, J. C. Perales, S. H. Kleinstein, E. D. Abel, K. L. Insogna, S. Feske, J. W. Locasale, M. W. Bosenberg, J. C. Rathmell, S. M. Kaech, Phosphoenolpyruvate is a metabolic checkpoint of anti-tumor T cell responses. *Cell* **162**, 1217–1228 (2015).
62. M. G. V. Heiden, J. W. Locasale, K. D. Swanson, H. Sharfi, G. J. Heffron, D. Amador-Noguez, H. R. Christofk, G. Wagner, J. D. Rabinowitz, J. M. Asara, L. C. Cantley, Evidence for an alternative glycolytic pathway in rapidly proliferating cells. *Science* **329**, 1492–1499 (2010).
63. D. J. Samuvel, K. P. Sundararaj, A. Nareika, M. F. Lopes-Virella, Y. Huang, Lactate Boosts TLR4 signaling and NF-κB pathway-mediated gene transcription in macrophages via monocarboxylate transporters and MD-2 up-regulation. *J. Immunol.* **182**, 2476–2484 (2009).
64. R. Haas, J. Smith, V. Rocher-Ros, S. Nadkarni, T. Montero-Melendez, F. D'Acquisto, E. J. Bland, M. Bombardieri, C. Pitzalis, M. Perretti, F. M. Marelli-Berg, C. Mauro, Lactate regulates metabolic and pro-inflammatory circuits in control of T cell migration and effector functions. *PLoS Biol.* **13**, e1002202 (2015).
65. E. M. Palsson-McDermott, A. M. Curtis, G. Goel, M. A. R. Lauterbach, F. J. Sheedy, L. E. Gleeson, M. W. M. van den Bosch, S. R. Quinn, R. Domingo-Fernandez, D. G. W. Johnston, J.-K. Jiang, W. J. Israelsen, J. Keane, C. Thomas, C. Clish, M. V. Heiden, R. J. Xavier, L. A. J. O'Neill, Pyruvate kinase M2 regulates Hif-1α activity and IL-1β induction and is a critical determinant of the Warburg effect in LPS-activated macrophages. *Cell Metab.* **21**, 65–80 (2015).
66. C.-H. Chang, J. D. Curtis, L. B. Maggi Jr., B. Faubert, A. V. Villarino, D. O'Sullivan, S. C.-C. Huang, G. J. W. van der Windt, J. Blagih, J. Qiu, J. D. Weber, E. J. Pearce, R. G. Jones, E. L. Pearce, Posttranscriptional control of T cell effector function by aerobic glycolysis. *Cell* **153**, 1239–1251 (2013).
67. A. Luengo, Z. Li, D. Y. Gui, L. B. Sullivan, M. Zagorulya, B. T. Do, R. Ferreira, A. Naamati, A. Ali, C. A. Lewis, C. J. Thomas, S. Spranger, N. J. Matheson, M. G. V. Heiden, Increased demand for NAD+ relative to ATP drives aerobic glycolysis. *Mol. Cell* **81**, 691–707.e6 (2021).
68. N. Yucel, Y. X. Wang, T. Mai, E. Porpiglia, P. J. Lund, G. Markov, B. A. Garcia, S. C. Bendall, M. Angelo, H. M. Blau, Glucose metabolism drives histone acetylation landscape transitions that dictate muscle stem cell function. *Cell Rep.* **27**, 3939–3955.e6 (2019).
69. P. Rocheteau, B. Gayraud-Morel, I. Siegl-Cachedenier, M. A. Blasco, S. Tajbakhsh, A subpopulation of adult skeletal muscle stem cells retains all template DNA strands after cell division. *Cell* **148**, 112–125 (2012).
70. J. G. Ryall, S. Dell'Orso, A. Derfoul, A. Juan, H. Zare, X. Feng, D. Clermont, M. Koulnis, G. Gutierrez-Cruz, M. Fulco, V. Sartorelli, The NAD+-dependent SIRT1 deacetylase translates a metabolic switch into regulatory epigenetics in skeletal muscle stem cells. *Cell Stem Cell* **16**, 171–183 (2015).
71. N. Pandey, B. E. Black, Rapid detection and signaling of DNA damage by PARP-1. *Trends Biochem. Sci.* **46**, 744–757 (2021).
72. A. R. Chaudhuri, A. Nussenzweig, The multifaceted roles of PARP1 in DNA repair and chromatin remodelling. *Nat. Rev. Mol. Cell Biol.* **18**, 610–621 (2017).
73. N. Xie, L. Zhang, W. Gao, C. Huang, P. E. Huber, X. Zhou, C. Li, G. Shen, B. Zou, NAD+ metabolism: Pathophysiologic mechanisms and therapeutic potential. *Signal Transduct. Target. Ther.* **5**, 227 (2020).
74. S. J. Pecher, A. B. Potthast, F. von Versen-Höynck, A. M. Das, Impact of short-term hypoxia on sirtuins as regulatory elements in HUVECs. *J. Clin. Med.* **9**, 2604 (2020).
75. K. Yan, Q. He, D. Lin, J. Liang, J. Chen, Z. Xie, Z. Chen, Promotion of NAD+ recycling by the hypoxia-induced shift in the lactate dehydrogenase isozyme profile reduces the senescence of human bone marrow-derived endothelial progenitor cells. *Free Radic. Biol. Med.* **208**, 88–102 (2023).
76. S. D. Kobayashi, F. R. DeLeo, Role of neutrophils in innate immunity: A systems biology-level approach. *Wiley Interdiscip. Rev. Syst.Biol. Med.* **1**, 309–333 (2009).
77. E. Chavakis, E. Choi, T. Chavakis, Novel aspects in the regulation of the leukocyte adhesion cascade. *Thromb. Haemost.* **102**, 191–197 (2009).
78. C. B. Peek, Metabolic implications of circadian–HIF crosstalk. *Trends Endocrinol. Metab.* **31**, 459–468 (2020).

79. M. Peiseler, P. Kubes, More friend than foe: The emerging role of neutrophils in tissue repair. *J. Clin. Investig.* **129**, 2629–2639 (2019).
80. C. F. P. Teixeira, S. R. Zamunér, J. P. Zuliani, C. M. Fernandes, M. A. Cruz-Hofling, I. Fernandes, F. Chaves, J. M. Gutiérrez, Neutrophils do not contribute to local tissue damage, but play a key role in skeletal muscle regeneration, in mice injected with Bothrops asper snake venom. *Muscle Nerve* **28**, 449–459 (2003).
81. R. A. Fielding, T. J. Manfredi, W. Ding, M. A. Fiatarone, W. J. Evans, J. G. Cannon, Acute phase response in exercise. III. Neutrophil and IL-1 beta accumulation in skeletal muscle. *Am. J. Physiol.-Regul., Integr. Comp. Physiol.* **265**, R166–R172 (1993).
82. J. G. Tidball, Inflammatory cell response to acute muscle injury. *Med. Sci. Sports Exerc.* **27**, 1022–1032 (1995).
83. P. F. Mercer, A. E. Williams, C. J. Scotton, R. J. José, M. Sulikowski, J. D. Moffatt, L. A. Murray, R. C. Chambers, Proteinase-activated receptor-1, CCL2, and CCL7 regulate acute neutrophilic lung inflammation. *Am. J. Respir. Cell Mol. Biol.* **50**, 144–157 (2014).
84. H. Lu, D. Huang, R. M. Ransohoff, L. Zhou, Acute skeletal muscle injury: CCL2 expression by both monocytes and injured muscle is required for repair. *FASEB J.* **25**, 3344–3355 (2011).
85. P. K. Shireman, V. Contreras-Shannon, O. Ochoa, B. P. Karia, J. E. Michalek, L. M. McManus, MCP-1 deficiency causes altered inflammation with impaired skeletal muscle regeneration. *J. Leukoc. Biol.* **81**, 775–785 (2007).
86. J. Zhang, Z. Xiao, C. Qu, W. Cui, X. Wang, J. Du, CD8 T cells are involved in skeletal muscle regeneration through facilitating MCP-1 secretion and Gr1high macrophage infiltration. *J. Immunol.* **193**, 5149–5160 (2014).
87. S. Chatterjee, H. Yin, D. Nam, Y. Li, K. Ma, Brain and muscle Arnt-like 1 promotes skeletal muscle regeneration through satellite cell expansion. *Exp. Cell Res.* **331**, 200–210 (2015).
88. J. Schindelin, I. Arganda-Carreras, E. Frise, V. Kaynig, M. Longair, T. Pietzsch, S. Preibisch, C. Rueden, S. Saalfeld, B. Schmid, J.-Y. Tinevez, D. J. White, V. Hartenstein, K. Eliceiri, P. Tomancak, A. Cardona, Fiji: An open-source platform for biological-image analysis. *Nat. Methods* **9**, 676–682 (2012).
89. A. Waisman, A. M. Norris, M. E. Costa, D. Kopinke, Automatic and unbiased segmentation and quantification of myofibers in skeletal muscle. *Sci. Rep.* **11**, 11793 (2021).
90. I. A. Barash, L. Mathew, A. F. Ryan, J. Chen, R. L. Lieber, Rapid muscle-specific gene expression changes after a single bout of eccentric contractions in the mouse. *Am. J. Physiol.-Cell Physiol.* **286**, C355–C364 (2004).
91. W. S. Pear, J. P. Miller, L. Xu, J. C. Pui, B. Soffer, R. C. Quackenbush, A. M. Pendergast, R. Bronson, J. C. Aster, M. L. Scott, D. Baltimore, Efficient and rapid induction of a chronic myelogenous leukemia-like myeloproliferative disease in mice receiving P210 bcr/abl-transduced bone marrow. *Blood* **92**, 3780–3792 (1998).
92. R. K. Naviaux, E. Costanzi, M. Haas, I. M. Verma, The pCL vector system: Rapid production of helper-free, high-titer, recombinant retroviruses. *J. Virol.* **70**, 5701–5705 (1996).
93. W. Zhang, W. Zeng, P. S. Wong, T. H. Cheung, Protocol for low-input proteomic analysis of in situ fixed adult murine muscle stem cells. *STAR Protoc.* **4**, 102750 (2023).
94. B. Gharaibeh, A. Lu, J. Tebbets, B. Zheng, J. Feduska, M. Crisan, B. Péault, J. Cummins, J. Huard, Isolation of a slowly adhering cell fraction containing stem cells from murine skeletal muscle by the preplate technique. *Nat. Protoc.* **3**, 1501–1509 (2008).
95. A. M. Bolger, M. Lohse, B. Usadel, Trimmomatic: A flexible trimmer for Illumina sequence data. *Bioinformatics* **30**, 2114–2120 (2014).
96. A. Dobin, C. A. Davis, F. Schlesinger, J. Drenkow, C. Zaleski, S. Jha, P. Batut, M. Chaisson, T. R. Gingeras, STAR: Ultrafast universal RNA-seq aligner. *Bioinformatics* **29**, 15–21 (2013).
97. B. Li, C. N. Dewey, RSEM: Accurate transcript quantification from RNA-seq data with or without a reference genome. *BMC Bioinformatics* **12**, 323 (2011).
98. M. I. Love, W. Huber, S. Anders, Moderated estimation of fold change and dispersion for RNA-seq data with DESeq2. *Genome Biol.* **15**, 550 (2014).
99. C. Soneson, M. I. Love, M. D. Robinson, Differential analyses for RNA-seq: Transcript-level estimates improve gene-level inferences. *F1000Res* **4**, 1521 (2015).
100. M. V. Kuleshov, M. R. Jones, A. D. Rouillard, N. F. Fernandez, Q. Duan, Z. Wang, S. Koplev, S. L. Jenkins, K. M. Jagodnik, A. Lachmann, M. G. McDermott, C. D. Monteiro, G. W. Gundersen, A. Ma'ayan, Enrichr: A comprehensive gene set enrichment analysis web server 2016 update. *Nucleic Acids Res.* **44**, W90–W97 (2016).
101. S. X. Ge, D. Jung, R. Yao, ShinyGO: A graphical gene-set enrichment tool for animals and plants. *Bioinformatics* **36**, 2628–2629 (2020).
102. Y. Hao, S. Hao, E. Andersen-Nissen, W. M. Mauck, S. Zheng, A. Butler, M. J. Lee, A. J. Wilk, C. Darby, M. Zager, P. Hoffman, M. Stoeckius, E. Papalexi, E. P. Mimitou, J. Jain, A. Srivastava, T. Stuart, L. M. Fleming, B. Yeung, A. J. Rogers, J. M. McElrath, C. A. Blish, R. Gottardo, P. Smibert, R. Satija, Integrated analysis of multimodal single-cell data. *Cell* **184**, 3573–3587.e29 (2021).
103. P.-L. Germain, A. Lun, C. G. Meixide, W. Macnair, M. D. Robinson, Doublet identification in single-cell sequencing data using scDblFinder. *F1000Res* **10**, 979 (2021).
104. T. Stuart, A. Butler, P. Hoffman, C. Hafemeister, E. Papalexi, W. M. Mauck III, Y. Hao, M. Stoeckius, P. Smibert, R. Satija, Comprehensive integration of single-cell data. *Cell* **177**, 1888–1902.e21 (2019).

Acknowledgments: We would like to thank J. Bass, G. Barish, S. Dayanidhi, and all members of the Peek, Bass, and Barish laboratories for helpful discussions. We thank the Transgenic and Targeted Mutagenesis Laboratory at Northwestern. During the preparation of this work, the author(s) used ChatGPT to improve clarity and grammar. After using this tool, the authors reviewed and edited the content as needed and take full responsibility for the content of the publication. **Funding:** This research was supported by the NIH NIDDK grants R01DK123358 and P30DK020595 (C.B.P)., the NIH NIAMS grant K08 AR081391 (I.R.), the US Department of Veterans Affairs grant IK6 RX003351 (R.L.L.), the NIH NIA grant 5P01AG049665-09 (N.S.C.), and the T32 HL076139-11 (C.R.R.). **Author contributions:** C.B.P., P.Z., and R.L.L. contributed to conceptualization, methodology, writing—review and editing, and supervision. C.B.P. and P.Z. additionally handled project administration and validation, with C.B.P. leading funding acquisition and P.Z. contributing to resources and data curation. P.Z., I.R., A.W., and Y.Z. contributed significantly to formal analysis and visualization, with I.R. also assisting in writing—original draft and resources. A.V.T., A.W.T.S., A.W., E.M.P., N.R.G., and A.K. participated in investigation and validation, with A.W.T.S., A.W., and E.M.P. also contributing to formal analysis. N.S.C. contributed to conceptualization and methodology, while C.R.R. provided support for resources and writing—review and editing. **Competing interests:** The authors declare that they have no competing interests. **Data and materials availability:** All data needed to evaluate the conclusions in the paper are present in the paper and/or the Supplementary Materials. The RNA-seq data are available in a public, open-access repository. All raw and processed files for each sample have been deposited at the National Center for Biotechnology Information (NCBI). The bulk RNA-seq data are available under accession number GSE278176, and the scRNA-seq data are available under accession number GSE278177. These data are publicly accessible without restrictions.

Submitted 3 June 2024
Accepted 30 January 2025
Published 5 March 2025
10.1126/sciadv.adq8538